

Article

Early Survival Prediction Framework in CD19-Specific CAR-T Cell Immunotherapy Using a Quantitative Systems Pharmacology Model

Anna Mueller-Schoell ^{1,2}, Nahum Puebla-Osorio ³, Robin Michelet ¹, Michael R. Green ³, Annette Künkele ^{4,5}, Wilhelm Huisinga ⁶, Paolo Strati ³, Beth Chasen ⁷, Sattva S. Neelapu ^{3,*}, Cassian Yee ^{8,9,*} and Charlotte Kloft ^{1,*}

- ¹ Department of Clinical Pharmacy and Biochemistry, Institute of Pharmacy, Freie Universitaet Berlin, 12169 Berlin, Germany; anna.mueller-schoell@fu-berlin.de (A.M.-S.); robin.michelet@fu-berlin.de (R.M.)
- ² Graduate Research Training Program PharMetriX, 12169 Berlin, Germany
- ³ Department of Lymphoma and Myeloma, Division of Cancer Medicine, The University of Texas MD Anderson Cancer Center, Houston, TX 77030, USA; npuebla@mdanderson.org (N.P.-O.); mgreen5@mdanderson.org (M.R.G.); PStrati@mdanderson.org (P.S.)
- ⁴ Department of Pediatric Oncology and Hematology, Charité–Universitätsmedizin Berlin, Corporate Member of Freie Universität Berlin, Humboldt–Universität zu Berlin, Augustenburger Platz 1, 1335 Berlin, Germany; annette.kuenkele@charite.de
- ⁵ German Cancer Consortium (DKTK), Partner Site Berlin, CCC (Campus Mitte), 10178 Berlin, Germany
- ⁶ Institute of Mathematics, University of Potsdam, 14476 Potsdam, Germany; huisinga@uni-potsdam.de
- ⁷ Department of Nuclear Medicine, Division of Diagnostic Imaging, The University of Texas MD Anderson Cancer Center, Houston, TX 77030, USA; Beth.Chasen@mdanderson.org
- ⁸ Department of Melanoma Medical Oncology, UT MD Anderson Cancer Center, Houston, TX 77030, USA
- ⁹ Department of Immunology, UT MD Anderson Cancer Center, Houston, TX 70030, USA
- * Correspondence: SNeelapu@mdanderson.org (S.S.N.); CYee@mdanderson.org (C.Y.); charlotte.kloft@fu-berlin.de (C.K.)



Citation: Mueller-Schoell, A.; Puebla-Osorio, N.; Michelet, R.; Green, M.R.; Künkele, A.; Huisinga, W.; Strati, P.; Chasen, B.; Neelapu, S.S.; Yee, C.; et al. Early Survival Prediction Framework in CD19-Specific CAR-T Cell Immunotherapy Using a Quantitative Systems Pharmacology Model. *Cancers* **2021**, *13*, 2782. <https://doi.org/10.3390/cancers13112782>

Academic Editors: Víctor M. Pérez-García, Lisette de Pillis, Philipp Altrock, Russell Rockne and Thomas Pabst

Received: 28 March 2021
Accepted: 28 May 2021
Published: 3 June 2021

Publisher's Note: MDPI stays neutral with regard to jurisdictional claims in published maps and institutional affiliations.



Copyright: © 2021 by the authors. Licensee MDPI, Basel, Switzerland. This article is an open access article distributed under the terms and conditions of the Creative Commons Attribution (CC BY) license (<https://creativecommons.org/licenses/by/4.0/>).

Simple Summary: Treatment with chimeric antigen receptor (CAR)-T cells has improved the prognosis of patients with non-Hodgkin lymphoma (NHL) substantially. Yet, as up to 60% of patients eventually relapse, insights into factors determining treatment response are highly warranted. We used mathematical modeling to characterize typical and individual concentration–time profiles of four different CAR-T cell subtypes and tumor burden in 19 NHL patients and investigated patient-/therapy-related factors associated with poor survival. A low CAR-T cell maximum expansion capacity and no previous autologous stem cell transplantation were associated with a poor prognosis. We next translated our most important model parameter into a clinical composite score, which leverages but does not require the use of the model. Based on our clinical data, we propose a clinical composite score cut-off value for early survival prediction. Additional data will be needed to update and refine the developed model and the proposed clinical composite score cut-off value.

Abstract: Chimeric antigen receptor (CAR)-T cell therapy has revolutionized treatment of relapsed/refractory non-Hodgkin lymphoma (NHL). However, since 36–60% of patients relapse, early response prediction is crucial. We present a novel population quantitative systems pharmacology model, integrating literature knowledge on physiology, immunology, and adoptive cell therapy together with 133 CAR-T cell phenotype, 1943 cytokine, and 48 metabolic tumor measurements. The model well described post-infusion concentrations of four CAR-T cell phenotypes and CD19⁺ metabolic tumor volume over 3 months after CAR-T cell infusion. Leveraging the model, we identified a low expansion subpopulation with significantly lower CAR-T cell expansion capacities amongst 19 NHL patients. Together with two patient-/therapy-related factors (autologous stem cell transplantation, CD4⁺/CD8⁺ T cells), the low expansion subpopulation explained 2/3 of the interindividual variability in the CAR-T cell expansion capacities. Moreover, the low expansion subpopulation had poor prognosis as only 1/4 of the low expansion subpopulation compared to 2/3 of the reference population were still alive after 24 months. We translated the expansion capacities into a clinical composite score (CCS) of ‘Maximum naïve CAR-T cell concentrations/Baseline tumor

burden' ratio and propose a CCS_{TN} -value > 0.00136 ($\text{cells} \cdot \mu\text{L}^{-1} \cdot \text{mL}^{-1}$) as predictor for survival. Once validated in a larger cohort, the model will foster refining survival prediction and solutions to enhance NHL CAR-T cell therapy response.

Keywords: chimeric antigen receptor T cells; non-Hodgkin lymphoma; CAR-T cells; mathematical modeling; pharmacometrics

1. Introduction

Chimeric antigen receptor (CAR)-T cell immunotherapy for relapsed or refractory B cell malignancies, such as acute lymphoblastic leukemia or non-Hodgkin lymphoma (NHL), has shown remarkable success [1–4]. Yet, in NHL, only 40–64% of patients show a durable response [1,5,6]. Thus, understanding the underlying factors of who will reach long-term response or not is essential. Several factors influence both CAR-T cell expansion and persistence, which are the two significant determinants of treatment response [7]. These factors include the design of the CAR construct [8], the manufacturing protocol [9], the frequency of functionally active T cells in the manufacturing and infusion products [10], the T cell phenotype [11,12], and the $CD4^+/CD8^+$ subset composition [12,13] in the infusion product, the tumor burden [10], the tumor microenvironment [14,15] and the dose and type of lymphodepleting chemotherapy [16,17]. Reported positive predictors for a long-term response are a high CAR-T cell maximum concentration (C_{\max}) [7,18,19], and a high area under the concentration–time curve in the first 28 days (AUC_{0-28d}) [7]. Factors such as a high fraction of central memory T cells (T_{CM}) or T memory stem cells (T_{SCM}) in manufacturing and infusion product have been linked to a high expansion and persistence [11,20]. Yet there is still sizeable unexplained variability in expansion, persistence, and response amongst patients, i.e., interindividual variability [7].

Previous top-down and bottom-up mathematical models of CAR-T cell therapy have described the kinetics of CAR-T cells [21], the quantitative relationship between CAR-affinity, antigen abundance, tumor cell depletion, and CAR-T cell expansion [22], and the kinetics and dynamics of effector and memory CAR-T cells and tumor cells [23,24]. While 'top-down' models refer to models developed based on observed new data, 'bottom-up' models are human physiology- and drug characteristics-based models [25]. A 'top-down' approach might describe the observed CAR-T cell kinetic data well, yet, little information is gained about the underlying mechanisms, and prediction of a concentration–time profile for a new individual might not be informative. Bottom-up approaches can add in-depth insight into CAR-T cell-tumor dynamics on a cellular level but might be too complex for clinical use and often underestimate the interindividual variability. To explain parts of this variability and identify mechanistically plausible predictors for long-term response, we developed a population quantitative systems pharmacology (QSP) model, characterizing the human kinetics of four CAR-T cell phenotypes and $CD19^+$ metabolic tumor volume and the dynamics of their interactions. Combining top-down and bottom-up approaches, our population QSP model uses prior information on CAR-T cell physiology together with in vivo data to inform unknown model parameter values and their interindividual variability [26]. Leveraging the model, we aimed to quantify different levels of variability in a clinical cohort of 19 NHL patients and identify significant influential factors on CAR-T cell expansion and survival. Finally, we sought to translate the model-estimated T cell expansion capacity into a clinical composite score to propose a cut-off value that allows survival prediction leveraging but not requiring the use of the model.

2. Materials and Methods

2.1. Patients and Treatment

Our clinical data contained a cohort of 24 adult patients with relapsed or refractory large B cell lymphoma treated with standard of care, axicabtagene ciloleucel, at MD

Anderson Cancer Center, Houston, Texas, USA. The study was approved by the MD Anderson Cancer Center's institutional review board and conducted in accordance with the principles of the Declaration of Helsinki. The 24 patients had different subtypes of non-Hodgkin lymphoma, such as diffuse large B cell lymphoma, primary mediastinal B cell lymphoma and transformed follicular lymphoma. Prior to CAR-T cell infusion on day 0, patients received a low-dose lymphodepleting chemotherapy consisting of fludarabine ($30 \text{ mg} \cdot \text{m}^{-2}$ body surface area per day) and cyclophosphamide ($500 \text{ mg} \cdot \text{m}^{-2}$ body surface area per day) on days -5 , -4 , and -3 . Further patient demographics and clinical characteristics prior to lymphodepleting chemotherapy are shown in detail in Supplementary Table S1. All patients received a single intravenous infusion of axicabtagene ciloleucel at a target dose of 2×10^6 CAR-T cell $\cdot \text{kg}^{-1}$ body weight. Of the 24 patients, we excluded five patients for the model analysis. Amongst these, one patient had no active disease during the whole study, for two patients no baseline metabolic tumor volume measurement was available, and for two patients, the staining steps during flow cytometry to determine CAR-T cell concentrations failed.

2.2. Tumor Size Measurements and Endpoint Assessment

Metabolic tumor volumes were assessed at baseline, after one month and three months after CAR-T cell infusion using fluorodeoxyglucose positron emission tomography computed tomography (PET-CT). Anti-tumor responses were assessed according to the 2014 Lugano classification [27]. Progression-free survival (PFS) was defined as the time from the start of the axicabtagene ciloleucel infusion to progression of disease, death, or last follow-up (whichever occurred first). Overall survival (OS) was defined as the time from the start of the axicabtagene ciloleucel infusion to death or last follow-up. Patients who were lost to follow-up were from overseas or other US states and did not return to MD Anderson Cancer Center for further monitoring.

2.3. CAR-T Cell Sampling, Detection, and Quantification

2.3.1. Sample Collection

Peripheral blood mononuclear cells (PBMCs) were isolated from blood samples by density gradient separation at days 7, 14, and 25–28 after CAR-T cell infusion and cryopreserved for batched analysis.

2.3.2. Cell-Free DNA Real-Time PCR

We used quantitative polymerase chain reaction (qPCR) to determine the DNA copy number of the CAR-T product in patient plasma samples (cell-free DNA, cfDNA). We used appropriate primers (FW—GGATTCGCCAGCCTCCAC; REV—AACTTGGCTCTTGGAG TTGT) and an endogenous probe (56—FAM/TCCCAGCCA/ZEN/CTCCAGACCCCTT/3IA BkFQ/) that correctly identified the chimeric region of CD19-CAR T product in CAR-T-transduced T cells. The DNA copy number from each mg of unknown cfDNA sample was determined using a 10-fold standard curve in which the value corresponding to the DNA copy number was calculated using regression analysis.

2.3.3. Flow Cytometry

PBMC were processed immediately after thawing; the cells were counted, analyzed for viability, and stained using fluorescently labeled antibodies for 30 min (we used antibody concentrations according to the manufacturer's recommendations) at room temperature. We used two antibody panels to measure the phenotype and activation of CAR-T CD4 and CD8 fractions. All cells were pre-treated with an anti-Fc block (130-059-901, Miltenyi Biotec, Bergisch Gladbach, Germany) and Aqua Live/Dead exclusion dye (L34957, Life Technologies, Carlsbad, CA, USA). The list of antibodies in each staining panel is as follows (the clone or reference number followed by the manufacturer's name is annotated in parenthesis): Cocktail 1—OX40 FITC (Cat No. 555837), anti-CAR T PE (KIP-1, BD Biosciences), ICOS PE-TR (C398.4A, BD Biosciences), CD127 PerCP Cy5.5 (HIL-7R-M21, BD

Biosciences, San Jose, CA, USA), CD69 APC (Cat No. 555533, BD Biosciences), CD28 APC-H7 (CD28.2, BD Biosciences), CD4 AF700 (RPA-T4, BD Biosciences), 4-1BB BV421 (4B4-1, BD Biosciences), CD14 BV605 (M5E2, BD Biosciences), CD8 BV650 (RPA-T8, BD Biosciences), CD3 BV711 (UCHT1, BD Biosciences), and PD-1 BV786 (EH12.1, BD Biosciences); and Cocktail 2—CD45RA FITC (Cat No. 555488, BD Biosciences), anti-CAR T PE (KIP-1, BD Biosciences), CD4 PE-TR (RPA-T4, BD Biosciences), CD16 PE-CY7 (3G8, BD Biosciences), CCR7 PerCP Cy5.5 (150503, BD Biosciences), CD25 APC-H7 (M-A251, BD Biosciences), CD27 AF700 (O323, Biolegend, Santiago, CA, USA), CD38 BV605 (HB7, BD Biosciences), CD8 BV650 (RPA-T8, BD Biosciences), CD3 BV711 (UCHT1, BD Biosciences), and CD56 BV786 (NCAM16.2, BD Biosciences). The acquisition of cytometric events varied and depended on the number and the viability of the PBMCs (this number fluctuated from 2×10^5 to 1×10^6 cells). We used a 12-color multiparametric approach using a 3-laser FACS Fortessa Cytometer (BD Biosciences, San Jose, CA, USA). We established a compensation matrix using the DiVa 6.1.1 software with the acquisition of single staining controls. We analyzed FCS files using FlowJo (BD Biosciences, San Jose, CA, USA). We plotted the total events on an SSC vs. FSC quadrant, and we excluded the doublets by gating out the cells on the periphery on the SSC vs. FSC plot (Supplementary Figure S1, top left). We excluded all dead cells by plotting SSC vs. Aqua (Supplementary Figure S1, top middle) and gated on the negative populations (live). We then re-plotted the live events using SSC vs. FSC and gated the lower and upper populations on the right (we did this because activated CAR-T cells appeared larger than normal lymphocytes) to select the lymphocyte populations (Supplementary Figure S1, top right). From the selected gate, we plotted SSC vs. CD3 (Supplementary Figure S1, bottom left); then, from the CD3⁺ populations, we plotted CD3 vs. CAR-T to discriminate all CD3⁺CAR-T⁻ from the CD3⁺CAR-T⁺ cells (Supplementary Figure S1, bottom middle). Using the CD3⁺CAR-T⁺ populations, we then plotted CD4 vs. CD8 to obtain single CD4⁺CAR-T⁺ and CD8⁺CAR-T⁺ populations (Supplementary Figure S1, bottom middle right). To define the phenotype, we plotted the CD4⁺ and CD8⁺ single-stained populations according to their level of expression of CD45RA vs. CCR7, thus, CD45RA⁺CCR7⁻ (T_{Eff}), CD45RA⁺CCR7⁺ (T_N), CD45RA⁻CCR7⁺ (T_{CM}), and CD45RA⁻CCR7⁻ (T_{EM}) (Supplementary Figure S1, bottom far right). We plotted each single subset vs. every single other marker included in each panel.

2.3.4. Cytokine Measurements

We measured plasma cytokines from CAR-T-infused patients at baseline (day 0), day 4, 7, 9, and 14 using the multiplex assay from Meso Scale Discovery system (Meso Scale 437 Diagnostics; Rockville, MD, USA). We ran 25 μ L samples in duplicate to identify Ang-1, Ang-2, EGF, G-CSF, GM-CSF, Granzyme B, GRO α (CXCL1), I-TAC (CXCL11), IFN- γ , IL-10, IL-15, IL-1RA, IL-1 α , IL-1 β , IL-2, IL-2RA, IL-3, IL-5, IL-6, IL-8, IP-10 (CXCL10), M-CSF, MCP-1(CCL2), MIG (CXCL9), MIP-1 α (CCL3), TNF- α , VEGF, and VWF, per the manufacturer's instructions.

2.4. Development of the CD19-Specific CAR-T Cell Quantitative Systems Pharmacology Model

We developed the population quantitative systems pharmacology CAR-T cell model by integrating previous knowledge on T cell physiology, adoptive cell therapy, and previously published mathematical immunotherapy models [28,29]. We aimed for our model to be as mechanistic as possible, allowing all parameters to have a physiological meaning while, to enable clinical use, maintaining simplicity following the principle of parsimony. We considered different sources of variability [26] by using a nonlinear mixed-effects modeling approach [30,31].

2.4.1. Nonlinear Mixed-Effects Modeling

A nonlinear mixed-effects model consists of three submodels [32]: the structural submodel, the statistical submodel, and the covariate submodel.

2.4.2. Structural Submodel

The structural submodel (including so called ‘fixed effects’) characterizes the typical concentration–time profile of one or more model species and is described using ordinary differential equations.

2.4.3. Statistical Submodel

The statistical submodel (including so-called ‘random effects’) captures different levels of unexplained variability around the parameters of the structural submodel and the observations. During development of the CAR-T cell quantitative systems pharmacology model, interindividual variability was evaluated on all structural model parameters using exponential interindividual variability models (Equation (1)).

$$\theta_{ik} = \theta_k \cdot e^{\eta_{ik}} \quad \eta_{ik} \sim N(0, \omega_k^2) \quad (1)$$

with the structural model parameter θ_k and individual model parameter θ_{ik} for individual $i = 1, \dots, N$ and model parameter $k = 1, \dots, N$. Individual model parameters on which interindividual variability was implemented were thus assumed to be log-normally distributed with η_{ik} values following a normal distribution with mean zero and variance ω_k^2 . To ease interpretation, the interindividual variability was expressed as coefficient of variation, using Equation (2) [32].

$$CV, \% = \sqrt{e^{\omega_k^2} - 1} \cdot 100 \quad (2)$$

Residual unexplained variability, quantifying the remaining unexplained variability after accounting for interindividual variability [32], was implemented for each model species using a log-transform-both sides approach [30,32] (Equation (3)), equivalent to an additive residual variability model on the log-scale.

$$\begin{aligned} \ln(Y_{ij}^{obs}) &= \ln(f(x_{ij}, \theta_i) \cdot e^{\varepsilon_{ij}}) \quad \varepsilon_{ij} \sim N(0, \sigma_{ij}^2) \\ \ln(Y_{ij}^{obs}) &= \ln(f(x_{ij}, \theta_i)) + \varepsilon_{ij} \quad \text{with} \quad \varepsilon_{ij} = \ln(Y_{ij}^{obs}) - \ln(Y_{ij}^{pred}) \end{aligned} \quad (3)$$

In Equation (3), the logarithm of individual observation Y_{ij}^{obs} for individual $i = 1, \dots, N$ and time point $j = 1, \dots, N$ are described as the logarithm of the function of independent design variable x_{ij} (for example sampling times), given the vector θ_i of model parameters for individual $i = 1, \dots, N$, and the residual unexplained variability parameter ε_{ij} . The residual unexplained variability for individual $i = 1, \dots, N$ at time point $j = 1, \dots, N$ quantifying the deviation between individual model prediction and observation, is implemented as an exponential function and assumed to be normally distributed with mean zero and variance σ_{ij}^2 . Applying a log-transformation to both the observation and the model predictions increases the numerical stability of the model, especially if observed concentrations range over several orders of magnitude. Analogous to Equation (2), the residual unexplained variability was expressed as coefficient of variation, using Equation (4).

$$CV, \% = \sqrt{e^{\sigma^2} - 1} \cdot 100 \quad (4)$$

2.4.4. Covariate Submodel

The covariate submodel (including ‘fixed effects’) aims to explain parts of the interindividual variability identified in the statistical submodel. The covariates (patient-, therapy-, or product-related characteristics) tested for significance during development of the CAR-T cell quantitative systems pharmacology model were pre-selected based on prior literature reports, physiological plausibility, and availability in our clinical study dataset. Exploratory graphical analyses were used to assess the potential size of the covariate effect and guide initial estimate selection.

2.4.5. Model Estimation, Parameter Precision, and Software

In the nonlinear mixed-effects approach ‘fixed-effects-’ and ‘random-effects’ parameters are simultaneously estimated by maximizing the likelihood [33,34]. The objective function value (OFV = $-2 \cdot \ln(\text{likelihood})$), a numeric criterion for quality of the model fit, decreases as the quality increases. Model selection for the CAR-T cell quantitative systems pharmacology model was thus based on the objective function value (OFV), parameter precision, and graphical goodness-of-fit evaluation. For the covariate submodel, we evaluated and refined our covariate selection by assessing changes with respect to parameter precision, model stability, individual model predictions, and significance of covariate inclusion using likelihood-ratio tests. At $\alpha = 0.05$, the inclusion of an additional covariate significantly improved model predictions if the OFV decreased by a value of 3.84 points.

If we observed a bi- or multimodal distribution instead of a normal distribution of the individual interindividual variability parameter estimates, suggesting separate subgroups of individuals, we investigated the implementation of a mixture model, allowing to define multiple subpopulations with different sets of typical parameter values. Even though the underlying factor discriminating the subpopulations, i.e., a covariate, might not be known, a mixture model allows to estimate the different parameter values of these subpopulations [35]. During model estimation including a mixture model, the typical values for the model parameters are estimated for each subpopulation. Furthermore, the proportion of individuals in each subpopulation and the most likely subpopulation for each individual are estimated.

To assess parameter uncertainty using standard errors, sampling importance resampling (SIR) [36], using the NONMEM generated covariance matrix to define a proposal distribution, was performed. More specifically, five iterations with 1000, 1000, 1000, 2000, and 2000 samples and 200, 400, 500, 1000, and 1000 resamples, respectively, were chosen. For easier interpretation, standard errors were reported in relation to the parameter estimate [30] as relative standard errors (RSEs). In general, RSEs $\leq 30\%$ for fixed-effects parameters and $\leq 50\%$ for random-effects parameters are considered adequate [30], however, higher RSEs might be acceptable based on the type of analysis, overall relevance of the parameter, and size of the dataset. All modeling activities were performed using the software NONMEM® Version 7.4.3 (ICON Development Solutions, Ellicott City, MD, USA), called through Perl speaks NONMEM (PsN) Version 3.6.2 [37], using the modeling workbench Pirana Version 2.9.7 (Certara, Princeton, NJ, USA) [38]. For parameter estimation, First-Order Conditional Estimation with Interaction was used. Pre- and post-processing and model evaluation were performed using R Version 3.5.1 (<https://www.R-project.org/> (accessed on 12 January 2021)) accessed through RStudio Version 1.2.1184 (<http://www.rstudio.com/> (accessed on 12 January 2021)), using packages plyr, dplyr, Xpose4, ggplot2, and scales.

2.5. Characterization of Patients in Different Model-Defined (Sub)Populations

During development of the CAR-T cell quantitative systems pharmacology model, two model-defined (sub)populations were identified based on their parameter values: a reference expansion population and a low expansion subpopulation. We investigated differences between both populations, which could potentially explain the observed differences in the model parameters. Continuous variables, i.e., baseline metabolic tumor volume and patient age, as well as frequencies of categorical covariates, i.e., disease type, previous/no previous ASCT and patient sex, were compared. Furthermore, observed and model-predicted cell kinetic parameters (i) maximum concentration of all CAR-T cells (C_{\max}), (ii) time at maximum concentration of all CAR-T cells (T_{\max}), (iii) area under the concentration–time curve from day 0 to day 28 (AUC_{0-28d}) of all CAR-T cells, and (iv) the ratio of C_{\max} of all CAR-T cells over baseline metabolic tumor volume, as a possible predictor for a good prognosis [39], were compared between both subpopulations. To assess statistical significance of differences between continuous covariate or cell kinetic parameter values, two-sided non-parametric Wilcoxon tests ($\alpha = 0.05$) using the function

‘compare_means’ of the R package *ggpubr* were performed. The results were visualized with box-whisker plots for continuous covariates and bar plots for categorical covariates using R package *ggplot2*.

2.6. Clinical Endpoints in Patients of Different Model-Defined (Sub)Populations

To compare clinical endpoints in different patient (sub)populations, Kaplan–Meier curves were generated and stratified for the respective variable (e.g., expansion subpopulation or previous/no previous ASCT) using the R packages *survival* and *survminer*. Log-rank tests ($\alpha = 0.05$) were used to assess if there was a significant difference between the curves. If we compared several strata within one plot, we performed pairwise comparisons in addition to the global log-rank test. A possible correlation between model parameter $V_{\max 1}$ and clinical composite score (CCS) C_{\max} /baseline metabolic tumor volume was assessed for each CAR-T cell phenotype and the sum of CAR-T cell phenotypes (T_{all}) using Pearson correlation tests through the ‘ggscatter’ function in the R package *ggpubr*. For the CAR-T cell phenotype for which the CCS showed the highest correlation with $V_{\max 1}$, we assessed an optimal cut-off value of the CCS for detecting patients in the low expansion subpopulation, by performing a receiver operating characteristic (ROC) curve analysis using the R packages *cutpointr* and *pROC* [40]. Next, we performed univariate cox-proportional hazard analyses using the R package *survival* to assess if the identified CCS cut-off value for the chosen CAR-T cell phenotype was a significant predictor for survival. We tested and confirmed the proportional hazard assumption using the function ‘cox.zph’ in the R *survival* package. Finally, the correlation between the CCS using flow cytometry and the CCS using qPCR was quantified using a Pearson-correlation test. The CCS_{qPCR} was compared between reference expansion population and low expansion subpopulation using a two-sided Wilcoxon test. Two additional previously digitized datasets [41], reporting C_{\max} (assessed by qPCR) and baseline tumor burden in CLL [42] and MM [43] patients, were digitized (Supplementary Figure S2). Next, CCS_{qPCR} were computed and the differences between patients with CR/PR and PD/NR assessed using two-sided Wilcoxon tests.

3. Results

3.1. The CD19-Specific CAR-T Cell Quantitative Systems Pharmacology Model

Based on previous reports regarding the impact of CAR-T cell phenotype composition on CAR-T cell in vivo expansion and persistence [44], we chose to describe each CAR-T cell phenotype measured in our clinical cohort (T_N , T_{CM} , T_{EM} , and T_{Eff}) as individual species. As a fifth species, we included CD19⁺ metabolic tumor volume as a pharmacodynamic component and a key driver of CAR-T cell expansion. To jointly describe typical profiles of concentrations of CAR-T cell phenotypes and CD19⁺ tumor volume across time and different layers of variability, we used nonlinear mixed-effects modeling.

3.1.1. Structural Submodel

The structural submodel of the nonlinear mixed-effects quantitative systems pharmacology model consisted of five species: naïve CAR-T cells (T_N), central memory CAR-T cells (T_{CM}), effector memory CAR-T cells (T_{EM}), terminally differentiated effector CAR-T cells (T_{Eff}), and CD19⁺ metabolic tumor volume (CD19⁺) (Figure 1). For the nonlinear processes describing T cell expansion upon tumor contact and tumor killing upon CAR-T cell contact, different functional forms were explored. While the numerator always consisted of the product $V_{\max, x} \cdot CD19^+ \cdot T_{\text{cell}}$, we tested three versions for the denominator, limiting the maximum expansion either by the respective T cell concentration, the metabolic tumor volume or both. For both terms, the form which described the data best was selected.

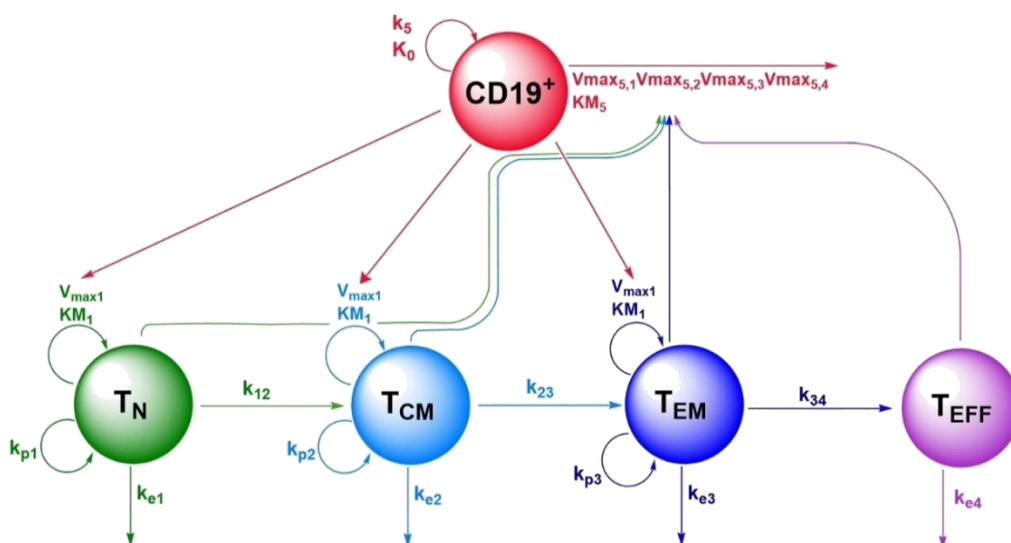


Figure 1. Schematic representation of the CD19-specific CAR-T cell population quantitative systems pharmacology model, describing kinetics and dynamics of the four CAR-T cell phenotypes and CD19⁺ tumor metabolic tumor volume. Legend: Non-red arrows pointing to the right describe differentiation processes. Non-red downward arrows represent cell death processes. Circular arrows represent proliferation processes. The red arrow pointing to the right represents CD19⁺ tumor death. Arrows pointing to parameter names indicate a positive impact on this parameter by the species of which the arrow is originating from. Abbreviations—T_N: naïve CAR-T cells; T_{CM}: central memory CAR-T cells; T_{EM}: effector memory CAR-T cells; T_{EFF}: effector CAR-T cells; CD19⁺: CD19⁺ metabolic tumor volume; k₁₂: rate constant for differentiation of T_N to T_{CM}; k₂₃: rate constant for differentiation of T_{CM} to T_{EM}; k₃₄: rate constant for differentiation of T_{EM} to T_{EFF}; k_{e1}: death rate constant for T_N; k_{e2}: death rate constant for T_{CM}; k_{e3}: death rate constant for T_{EM}; k_{e4}: death rate constant for T_{EFF}; k_{p1}: homeostatic proliferation rate constant for T_N; k_{p2}: homeostatic proliferation rate constant for T_{CM}; k_{p3}: homeostatic proliferation rate constant for T_{EM}; V_{max1}: maximum expansion rate per mL tumor volume of T_N, T_{CM} and T_{EM} upon tumor contact; KM₁: T_N, T_{CM} and T_{EM} concentration at half-maximum expansion of T_N, T_{CM} and T_{EM}; V_{max5,1}: maximum killing rate of metabolic tumor volume by T_N; V_{max5,2} maximum killing rate of metabolic tumor volume by T_{CM}; V_{max5,3}: maximum killing rate of metabolic tumor volume by T_{EM}; V_{max5,4}: maximum killing rate of metabolic tumor volume by T_{EFF}; KM₅: metabolic tumor volume at half-maximum killing rate; k₅: proliferation rate constant of metabolic tumor volume; K₀: maximum tumor volume observable (tumor carrying capacity).

We described the lineage relationship of the four CAR-T cell phenotypes according to the progressive differentiation model, which postulates the differentiation of naïve T cells via memory T cells to terminally differentiated effector T cells [45,46].

Naïve CAR-T Cells (T_N)

Upon contact with CD19⁺ tumor cells, we modeled T_N to expand with maximum expansion rate per mL tumor volume V_{max1} and naïve T cell concentration at half-maximum expansion rate KM₁ (1.13 cells·μL⁻¹, relative standard error (RSE): 22%). Independent of expansion upon tumor cell contact, T_N undergo homeostatic proliferation with a first-order rate constant k_{p1} (0.0005·day⁻¹) [47]. Furthermore, we described T_N to differentiate into T_{CM} with the first-order rate constant k₁₂ (0.140·day⁻¹, RSE: 9%) and undergo apoptosis corresponding to a typical lifespan of 1/k_{e1} (1/0.0104·day⁻¹ = 96 days, RSE: 13%) days. The resulting typical profile for T_N is given by Equation (5).

$$\frac{d}{dt}T_N = \frac{V_{max1} \cdot CD19^+ \cdot T_N}{KM_1 + T_N} + k_{p1} \cdot T_N - k_{12} \cdot T_N - k_{e1} \cdot T_N \tag{5}$$

Central Memory CAR-T Cells (T_{CM})

Analogous to T_N, we modeled T_{CM} to expand upon tumor contact with the same Michaelis–Menten parameters V_{max1} and KM₁ and to undergo homeostatic proliferation

with the rate constant kp_2 ($0.007 \cdot \text{day}^{-1}$) [47]. Moreover, we described concentrations of T_{CM} to increase by differentiation of T_N with the rate constant k_{12} . In line with the progressive differentiation model, concentrations of T_{CM} were described to decrease due to differentiation into T_{EM} with the rate constant k_{23} ($0.191 \cdot \text{day}^{-1}$, RSE: 11%) or apoptosis after a typical lifespan of $1/k_{e2}$ ($1/0.0104 \cdot \text{day}^{-1} = 96$ days, RSE: 13%) days. The resulting typical profile of T_{CM} is given by Equation (6).

$$\frac{d}{dt}T_{CM} = \frac{V_{\max 1} \cdot CD19^+ \cdot T_{CM}}{KM_1 + T_{CM}} + kp_2 \cdot T_{CM} + k_{12} \cdot T_N - k_{23} \cdot T_{CM} - k_{e2} \cdot T_{CM} \quad (6)$$

Effector Memory CAR-T Cells (T_{EM})

Analogous to T_N and T_{CM} , we modeled T_{EM} cells to expand upon tumor contact in a nonlinear process with the parameters $V_{\max 1}$ and KM_1 . In addition, T_{EM} cells were described to undergo linear homeostatic proliferation with the rate constant kp_3 ($0.007 \cdot \text{day}^{-1}$) [47] and to be formed via differentiation of T_{CM} with the rate constant k_{23} . Moreover, we described T_{EM} to differentiate into T_{Eff} with the rate constant k_{34} ($0.355 \cdot \text{day}^{-1}$, RSE: 13%) and to undergo apoptosis after a typical lifespan of $1/k_{e3}$ ($1/0.0104 \cdot \text{day}^{-1} = 96$ days, RSE: 13%) days. The resulting typical profile of T_{EM} is given by Equation (7):

$$\frac{d}{dt}T_{EM} = \frac{V_{\max 1} \cdot CD19^+ \cdot T_{EM}}{KM_1 + T_{EM}} + kp_3 \cdot T_{EM} + k_{23} \cdot T_{CM} - k_{34} \cdot T_{EM} - k_{e3} \cdot T_{EM} \quad (7)$$

Terminally Differentiated Effector CAR-T Cells (T_{Eff})

In contrast to naïve and memory T cells, we considered T_{Eff} cells unable to expand further in response to tumor contact or as homeostatic proliferation. We still considered them to be formed by differentiation of T_{EM} with the rate constant k_{34} . In line with previous findings [21,48], as shown in the high estimate for k_{e4} , we approximated that a high fraction of T_{Eff} will die each day ($0.518 \cdot \text{day}^{-1}$, RSE: 13%). The resulting typical profile of T_{Eff} is given by Equation (8).

$$\frac{d}{dt}T_{Eff} = k_{34} \cdot T_{EM} - k_{e4} \cdot T_{Eff} \quad (8)$$

CD19⁺ Metabolic Tumor Volume (CD19⁺)

We modeled CD19⁺ metabolic tumor volume growth with a logistic growth function [28] with growth parameter k_5 (0.0023 day^{-1}) and carrying capacity K_0 (5000 mL), which represents the highest metabolic tumor volume observable (Equation (9)). Tumor cell killing by the different CAR-T cell phenotypes was adapted from a previously published tumor immune reaction mathematical model [28] as a nonlinear process with maximum killing rate $V_{\max 5,x}$ (with $x = 1-4$ representing the four CAR-T cell phenotypes in the order naïve, central memory, effector memory and effector), and metabolic tumor volume at half-maximum killing rate KM_5 (276 mL, RSE: 33%). While for parameter $V_{\max 5,2}$, the maximum killing rate for T_{CM} was estimated ($4.04 \text{ mL} \cdot \text{day}^{-1} \cdot (\text{cells} \cdot \mu\text{L}^{-1})^{-1}$, RSE: 39%), the maximum killing rates for the other T cell phenotypes were fixed based on the estimate for $V_{\max 5,2}$ and fractional changes in killing capacities extracted from a digitized plot showing in vitro killing capacities of different CAR-T cell phenotypes [49].

$$\begin{aligned} \frac{d}{dt}CD19^+ = k_5 \cdot & \left(1 - \frac{CD19^+}{K_0}\right) \cdot CD19^+ - \frac{V_{\max 5,1} \cdot T_N \cdot CD19^+}{KM_5 + CD19^+} \\ & - \frac{V_{\max 5,2} \cdot T_{CM} \cdot CD19^+}{KM_5 + CD19^+} - \frac{V_{\max 5,3} \cdot T_{EM} \cdot CD19^+}{KM_5 + CD19^+} \\ & - \frac{V_{\max 5,4} \cdot T_{Eff} \cdot CD19^+}{KM_5 + CD19^+} \end{aligned} \quad (9)$$

3.1.2. Statistical Submodel

We implemented interindividual variability parameters on $V_{\max 1}$ (446% CV) and $V_{\max 5,2}$ (307% CV) using Equation (1). The implementation of interindividual variability parameters on other structural submodel parameters was not supported by the dataset. Applying Equations (5)–(9) with the estimated parameter values to the measured concentrations of (i) the four CAR-T cell phenotypes and (ii) metabolic tumor volumes in our clinical dataset ($n = 19$ patients, Table S1), population and individual model predictions were in line with observed values for the majority of individuals. However, for some patients, typical predictions exceeded the measured T cell concentrations by up to 270-fold. A common feature of these patients was that T cells failed to expand as expected based on the high baseline tumor burden. Furthermore, we observed a bimodal distribution of individual $V_{\max 1, \text{base}}$ estimates. Based on this observation, we used a mixture model to investigate the presence of two subpopulations with separate estimates for $V_{\max 1, \text{base}}$. We precisely estimated 20% (RSE: 11%) ($n = 4$) of patients to belong to a low expansion subpopulation with a significantly reduced (by 92%, $p = 0.0043$) typical value for $V_{\max 1, \text{base}}$ ($V_{\max 1, \text{base}, \text{low}}$: $0.000700 \text{ (cells} \cdot \mu\text{L}^{-1}) \cdot \text{day}^{-1} \cdot \text{mL}^{-1}$, RSE: 17%) compared to the reference population ($V_{\max 1, \text{base}, \text{ref}}$: $0.00846 \text{ (cells} \cdot \mu\text{L}^{-1}) \cdot \text{day}^{-1} \cdot \text{mL}^{-1}$, RSE: 36%). The mixture model's implementation significantly improved and aligned typical and individual predictions for the low expansion subpopulation (Supplementary Figure S3).

3.1.3. Covariate Submodel

We pre-selected a previous ASCT, the ratio of CD4⁺ to CD8⁺ CAR-T cells on day seven and the concentrations of IL-2 and IL-15 for evaluation as covariates on model parameter $V_{\max 1, \text{base}}$. Furthermore, we pre-selected tumor type and concentrations of Granzyme-B, TNF α , and IFN- γ on day seven for evaluation on model parameter $V_{\max 5,2}$. Ratios of CD4⁺ over CD8⁺ CAR-T cells and cytokine concentrations were additionally available at baseline and on days four, nine, 14 and 28. However, measurements were not available for all patients at all time points. As measurements were available for 18 of 19 patients on day seven, we chose this time point for implementation.

We identified two significant covariates on the baseline maximum expansion rates $V_{\max 1, \text{base}, \text{ref}}$ and $V_{\max 1, \text{base}, \text{low}}$. A previous ASCT was incorporated as dichotomous covariate (ASCT = 0: no previous ASCT, ASCT = 1: previous ASCT) and the change in $V_{\max 1, \text{base}}$ due to a previous ASCT was implemented using a fractional change model (ASCT $_{V_{\max 1}}$: 2.53, RSE: 31%, translating into a 3.53-fold higher $V_{\max 1, \text{base}}$ value in patients with a previous ASCT). Of note, the covariate effect for a previous ASCT was estimated for all patients simultaneously using their respective $V_{\max 1, \text{base}}$ value ($V_{\max 1, \text{base}, \text{ref}}$ or $V_{\max 1, \text{base}, \text{low}}$) instead of estimating separate effects of a previous ASCT for $V_{\max 1, \text{base}, \text{ref}}$ and $V_{\max 1, \text{base}, \text{low}}$. The second covariate, the ratio of CD4⁺/CD8⁺ CAR-T cells at day seven (CAR⁺CD4/CD8_{day7}), was implemented on $V_{\max 1, \text{base}, \text{ref}}$ using a power function. An increasing ratio of CD4/CD8⁺ CAR-T cells at day seven was associated with a moderate decrease in $V_{\max 1, \text{base}, \text{ref}}$ (CD4/CD8_{exp}: -0.385 , RSE: 45%). As for the low expansion subpopulation, an exploratory graphical analysis showed that only a previous ASCT but not the ratio of CD4⁺/CD8⁺ CAR-T cells at day seven was influential on the baseline maximum expansion capacity $V_{\max 1, \text{base}, \text{low}}$ (Supplementary Figure S4) and only a previous ASCT remained as covariate on $V_{\max 1, \text{base}, \text{low}}$. There was no significant relationship between other possible covariates and $V_{\max 1, \text{base}}$. The final equations for $V_{\max 1}$ applicable to the reference and low expansion (sub)populations are shown in Equations (10) and (11), respectively. In these equations, $V_{\max 1, \text{ref}}$ and $V_{\max 1, \text{low}}$ are the maximum expansion rates per mL metabolic tumor volume in the reference and the low expansion (sub)population, respectively, based on (i) the typical maximum expansion rates per mL metabolic tumor volume in the reference population ($V_{\max 1, \text{base}, \text{ref}}$) or the low expansion subpopulation ($V_{\max 1, \text{base}, \text{low}}$), (ii) the fractional change in $V_{\max 1, \text{base}, \text{ref}}$ or $V_{\max 1, \text{base}, \text{low}}$ due to a previous ASCT (ASCT $_{V_{\max 1}}$), and (iii) for the reference population the change in $V_{\max 1, \text{base}, \text{ref}}$ based

on the measured ratio of CD4⁺/CD8⁺ CAR-T cells on day 7 ($\text{CAR}^+\text{CD4}/\text{CD8}_{\text{day7}}$) to the power of model-estimated exponent CD4/CD8_{exp}.

$$V_{\text{max1,ref}} = V_{\text{max1,base,ref}} \cdot (1 + \text{ASCT}_{V_{\text{max1}}} \cdot \text{ASCT}) \cdot (\text{CAR}^+\text{CD4}/\text{CD8}_{\text{day7}})^{\text{CD4}/\text{CD8}_{\text{exp}}} \quad (10)$$

$$V_{\text{max1,low}} = V_{\text{max1,base,low}} \cdot (1 + \text{ASCT}_{V_{\text{max1}}} \cdot \text{ASCT}) \quad (11)$$

Upon implementation of mixture model and covariates, the interindividual variability in $V_{\text{max1,base,ref}}$ was substantially reduced from 446% to 150% (RSE: 19%) CV. The interindividual variability in $V_{\text{max1,base,low}}$ was negligible and not included in the model. Final model predictions for concentration–time profiles of all T cell phenotypes and metabolic tumor volume corresponded well with the observations as shown in goodness of fit plots (Figure 2) and observations overlaid with model predictions (Figure 3).

Both Figures 2 and 3 show individual and typical predictions, which are model predictions considering and not considering unexplained interindividual variability, respectively. Differences in typical predictions among individuals arose due to the explained interindividual variability already incorporated in the ‘fixed-effects’ parameters, such as different metabolic tumor volumes as model input or covariate effects. The adequate alignment of typical and individual predictions with the measured concentrations indicated no missed important process in the structural model and/or no missing covariate. After accounting for interindividual variability we quantified the remaining unexplained variability with residual unexplained variability parameters (CV: 59% (RSE: 11%), 86% (RSE: 9%), 120% (RSE: 9%), 71% (RSE: 10%), and 115% (RSE: 12%) for T_N , T_{CM} , T_{EM} , T_{Eff} , and CD19⁺ tumor, respectively).

3.1.4. Model Estimation and Parameter Precision

No information regarding initial CAR-T cell concentrations in the individual infusion products was available. We mainly focused on CAR-T cell expansion, which is primarily influenced by the tumor burden and the intrinsic CAR-T cell expansion capacity. Thus, we decided to discount the initial distribution phase and assume a low dose of 0.1 cells· μL^{-1} per phenotype as dose. It is plausible to observe this concentration after the initial distribution phase post-infusion. A subsequent sensitivity analysis showed that a ten-fold change of this value had a minor impact on the time of maximum T cell concentration but not on the maximum concentration itself (Supplementary Figure S5), which is in line with previously published data [13]. In addition, our model’s ability to describe the observed data well using the imputed doses supports previous findings of CAR-T cell doses not being predictive of expansion or response [3,18,41].

Most of the parameter values were estimated based on clinical data of CAR-T cell concentrations and metabolic tumor volume. However, using our clinical data, not all model parameters could be estimated: As our data only contained measurements of metabolic tumor volume in the presence of CAR-T cells, parameters k_5 and K_0 , which describe undisturbed tumor growth and the largest tumor volume observable, were not identifiable and fixed to plausible values. Similarly, homeostatic proliferation rate constants were set to literature values [47] as we performed our CAR-T cell concentration measurements during the rapid expansion phase. As the proliferation in response to target engagement is much faster than homeostatic proliferation, homeostatic proliferation rate constants were unidentifiable. Finally, death rate constants for T_N , T_{CM} and T_{EM} were unidentifiable and fixed based on the estimated death rate constant for T_{Eff} and the relationship between death rate constants of short- and long-lived cells (2%), according to Stein et al. [21]. Final model parameter values are shown in Table 1.

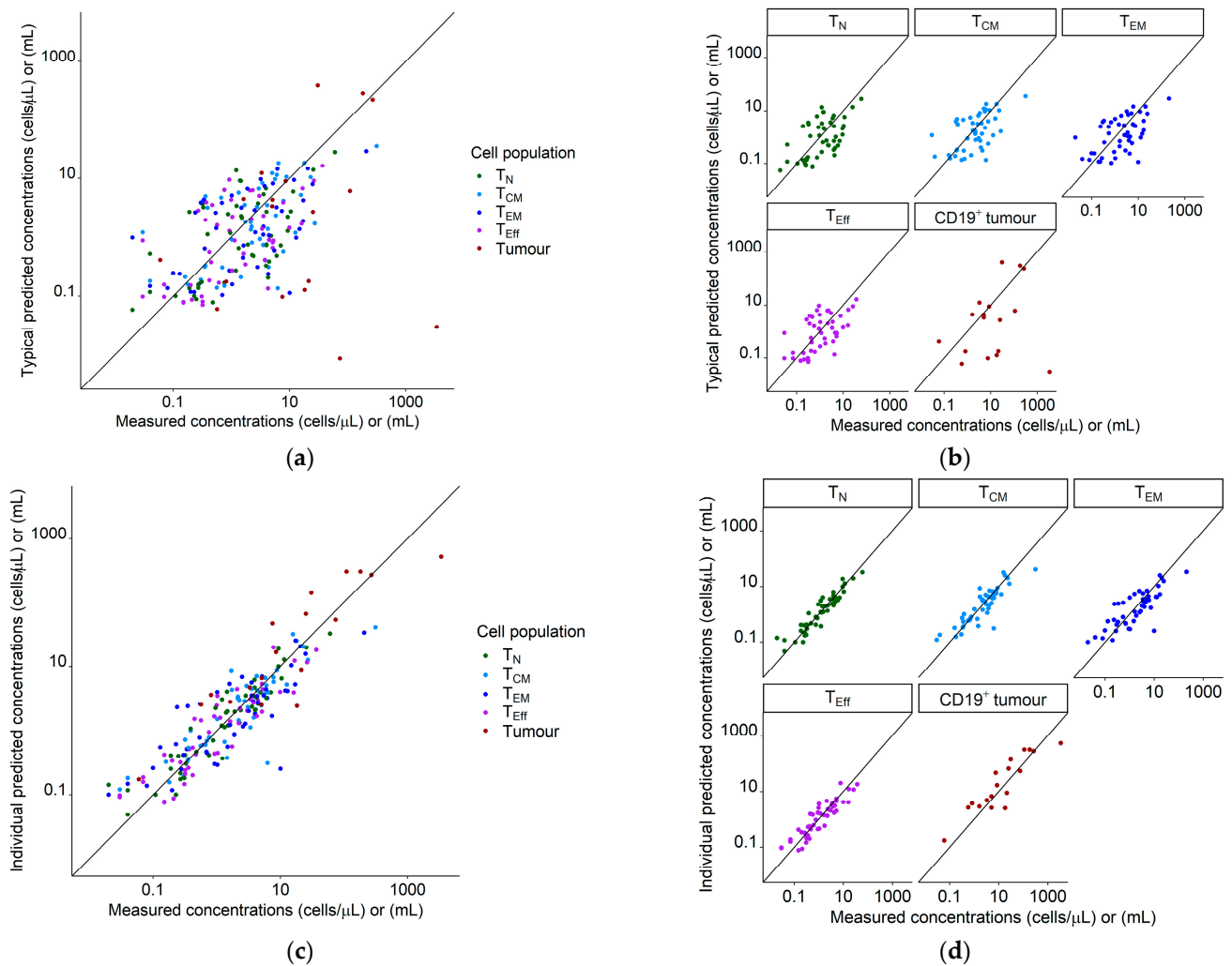


Figure 2. Goodness of fit plots for the population quantitative systems pharmacology model using our clinical dataset of 19 patients. Legend: (a) Typical predictions (not considering interindividual variability) vs. measured concentrations/volumes for all species; (b) typical predictions (not considering interindividual variability) vs. measured concentrations/volumes, stratified for species; (c) individual predictions vs. measured concentrations for all species; (d) individual predictions vs. measured concentrations, stratified for species. Diagonal line: Line of identity. Tumor measurements marked as a complete response were set to a value of 0 mL and are not shown. Abbreviations— T_N : naïve T cells, T_{CM} : central memory T cells, T_{EM} : effector memory T cells, T_{Eff} : effector T cells, $CD19^+$ tumour: $CD19^+$ metabolic tumor volume.

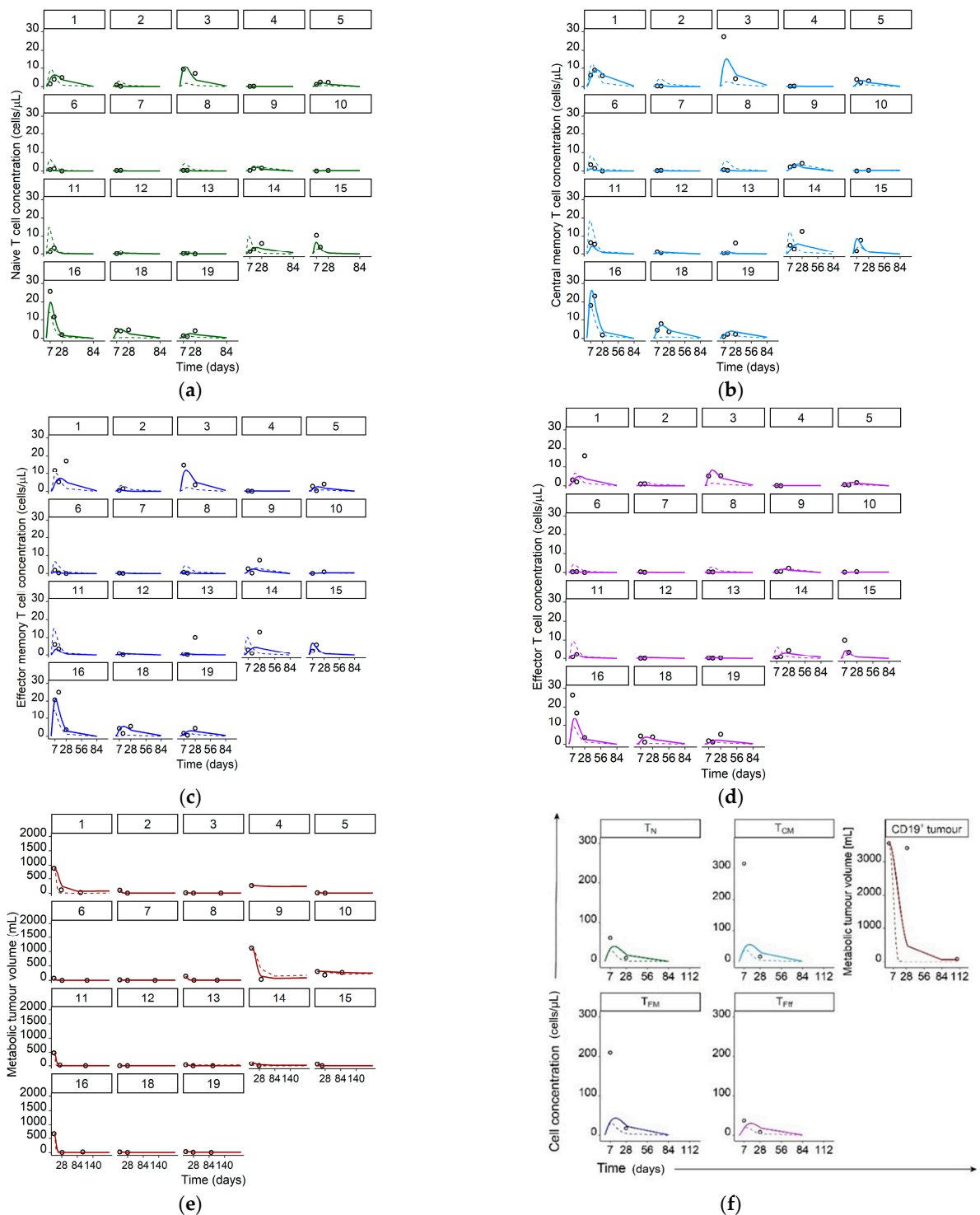


Figure 3. Measured T cell concentrations/metabolic tumor volumes (data points) and simulated typical (dashed lines) and individual (solid lines) model predictions for individual patients 1–16, and 18–19 in panels a–e and, as concentrations/volumes of all species were significantly higher, for patient 17 in separate panel (f). Legend: (a) Naive CAR-T cells; (b) Central memory CAR-T cells; (c) Effector memory CAR-T cells; (d) Effector CAR-T cells; (e) CD19⁺ metabolic tumor volume; (f) Concentrations of naive, central memory, effector memory, and effector CAR-T cells as well as CD19⁺ metabolic tumor volume for patient 17. Abbreviations—T_N: naive CAR-T cells, T_{CM}: central memory CAR-T cells, T_{EM}: effector memory CAR-T cells, T_{Eff}: effector CAR-T cells, CD19⁺ tumor: CD19⁺ metabolic tumor volume.

Table 1. Final parameter estimates for the CD19-specific CAR-T cell quantitative systems pharmacology model.

Parameter (Unit)	Description	Estimate	RSE or Literature Source
$V_{\max 1, \text{base, ref}}$ [(cells· μL^{-1}) ·day $^{-1}$ ·mL $^{-1}$]	Maximum expansion rate per mL tumor volume of T_N , T_{CM} , and T_{EM} for the reference expansion population without previous ASCT and a CD4 $^+$ /CD8 $^+$ CAR-T cell ratio at day seven of 1	0.00846	36%
$V_{\max 1, \text{base, low}}$ [(cells· μL^{-1}) ·day $^{-1}$ ·mL $^{-1}$]	Maximum expansion rate per mL tumor volume of T_N , T_{CM} , and T_{EM} for the low expansion subpopulation without previous ASCT	0.000700	17%
ASCT $V_{\max 1}$ § (–)	Fractional change in $V_{\max 1, \text{base, ref}}$ or $V_{\max 1, \text{base, low}}$ due to a previous ASCT	2.53	31%
CD4/CD8 $_{\text{exp}}$ † (–)	Fractional change in $V_{\max 1, \text{base, ref}}$ due to a change of the CD4 $^+$ /CD8 $^+$ CAR-T cell ratio on day seven from a value of 1	–0.385	45%
KM_1 (cells· μL^{-1})	T_N , T_{CM} , or T_{EM} concentration at half-maximum expansion of T_N , T_{CM} , or T_{EM}	1.13	22%
kp $_1$ (day $^{-1}$)	Homeostatic proliferation rate constant for T_N	0.0005	[47]
kp $_2$ (day $^{-1}$)	Homeostatic proliferation rate constant for T_{CM}	0.007	[47]
kp $_3$ (day $^{-1}$)	Homeostatic proliferation rate constant for T_{EM}	0.007	[47]
k $_{12}$ (day $^{-1}$)	Rate constant for differentiation of T_N to T_{CM}	0.140	9%
k $_{23}$ (day $^{-1}$)	Rate constant for differentiation of T_{CM} to T_{EM}	0.191	11%
k $_{34}$ (day $^{-1}$)	Rate constant for differentiation of T_{EM} to T_{Eff}	0.355	13%
ke $_1$ (day $^{-1}$)	Death rate constant for T_N	0.0104 ‡	13%
ke $_2$ (day $^{-1}$)	Death rate constant for T_{CM}	0.0104 ‡	13%
ke $_3$ (day $^{-1}$)	Death rate constant for T_{EM}	0.0104 ‡	13%
ke $_4$ (day $^{-1}$)	Death rate constant for T_{Eff}	0.518	13%
$V_{\max 5, 1}$ [mL·day $^{-1}$ ·(cells· μL^{-1}) $^{-1}$]	Maximum killing rate of metabolic tumor volume by T_N	2.57 *	39%
$V_{\max 5, 2}$ [mL·day $^{-1}$ ·(cells· μL^{-1}) $^{-1}$]	Maximum killing rate of metabolic tumor volume by T_{CM}	4.04	39%
$V_{\max 5, 3}$ [mL·day $^{-1}$ ·(cells· μL^{-1}) $^{-1}$]	Maximum killing rate of metabolic tumor volume by T_{EM}	3.78 *	39%
$V_{\max 5, 4}$ [mL·day $^{-1}$ ·(cells· μL^{-1}) $^{-1}$]	Maximum killing rate of metabolic tumor volume by T_{Eff}	4.24 *	39%
KM_5 (mL)	Metabolic tumor volume at half-maximum killing rate	276	33%
K_0 (mL)	Maximum tumor volume observable (tumor carrying capacity)	5000	-
k $_5$ (day $^{-1}$)	Proliferation rate constant of metabolic tumor volume	0.0023	-
MIXP (–)	Estimated proportion of patients in the reference population using the mixture model	0.803	11%
IIV $V_{\max 1, \text{base, ref}}$	Interindividual variability in $V_{\max 1, \text{base, ref}}$	150% CV	19%
IIV $V_{\max 5, 2}$	Interindividual variability in $V_{\max 5, 2}$	307% CV	19%
RUV T_N	Residual unexplained variability in observed T_N concentrations	59.1% CV	11%
RUV T_{CM}	Residual unexplained variability in observed T_{CM} concentrations	85.9% CV	9%
RUV T_{EM}	Residual unexplained variability in observed T_{EM} concentrations	120% CV	9%
RUV T_{Eff}	Residual unexplained variability in observed T_{Eff} concentrations	70.6% CV	10%
RUV CD19 $^+$ tumor	Residual unexplained variability in observed metabolic tumor volumes	115% CV	12%

IIV: interindividual variability; RSE: relative standard error, % = (standard error/estimate)·100; §: implemented as fractional change covariate model, †: implemented as power covariate model; ‡ derived using the estimated death rate constant for effector T cells ke $_4$ and the relationship between death rate constants of short- and long-lived T cells in the publication by Stein et al. [21]; * derived using the estimated maximum killing rate of metabolic tumor volume by T_{CM} and the digitized relationships of tumor cell killing rates in the publication by Schmueck-Henneresse et al. [49].

3.2. Characterization of Patients in Different Model-Defined (Sub)Populations

To explore reasons for the differences between the reference ($n = 15$) and low expansion ($n = 4$) (sub)populations, we compared clinical characteristics amongst patients in the respective groups: the low expansion subpopulation showed a significantly higher baseline metabolic tumor volume (median: 712 mL, range: 264 mL–3555 mL vs. median: 64.1 mL, range: 2.54 mL–894 mL, $p = 0.019$, Figure 4a).

The median patient age (48 years vs. 58 years) (Figure 4b) and the number of previous therapies (5 vs. 5) were similar in both (sub)populations. In addition, males and females were similarly distributed in the reference population and the low expansion subpopulation [females: 83% and 17%, respectively; males: 77% and 23%, respectively]. The patients in the reference population ($n = 15$) had diffuse large B cell lymphoma (DLBCL; 60% [$n = 9$]), transformed follicular lymphoma (TFL; 33.3% [$n = 5$]), and primary mediastinal lymphoma (PMBCL; 6.67% [$n = 1$]). Around 50% ($n = 2$) of the low expansion subpopulation ($n = 4$) had DLBCL, 25% ($n = 1$) had TFL, and 25% ($n = 1$) had PMBCL (Figure 4c). While 40% ($n = 6$) of patients in the reference expansion population ($n = 15$) had received a previous ASCT, only 25% ($n = 1$) of the patients in the low expansion subpopulation ($n = 4$) had (Figure 4d).

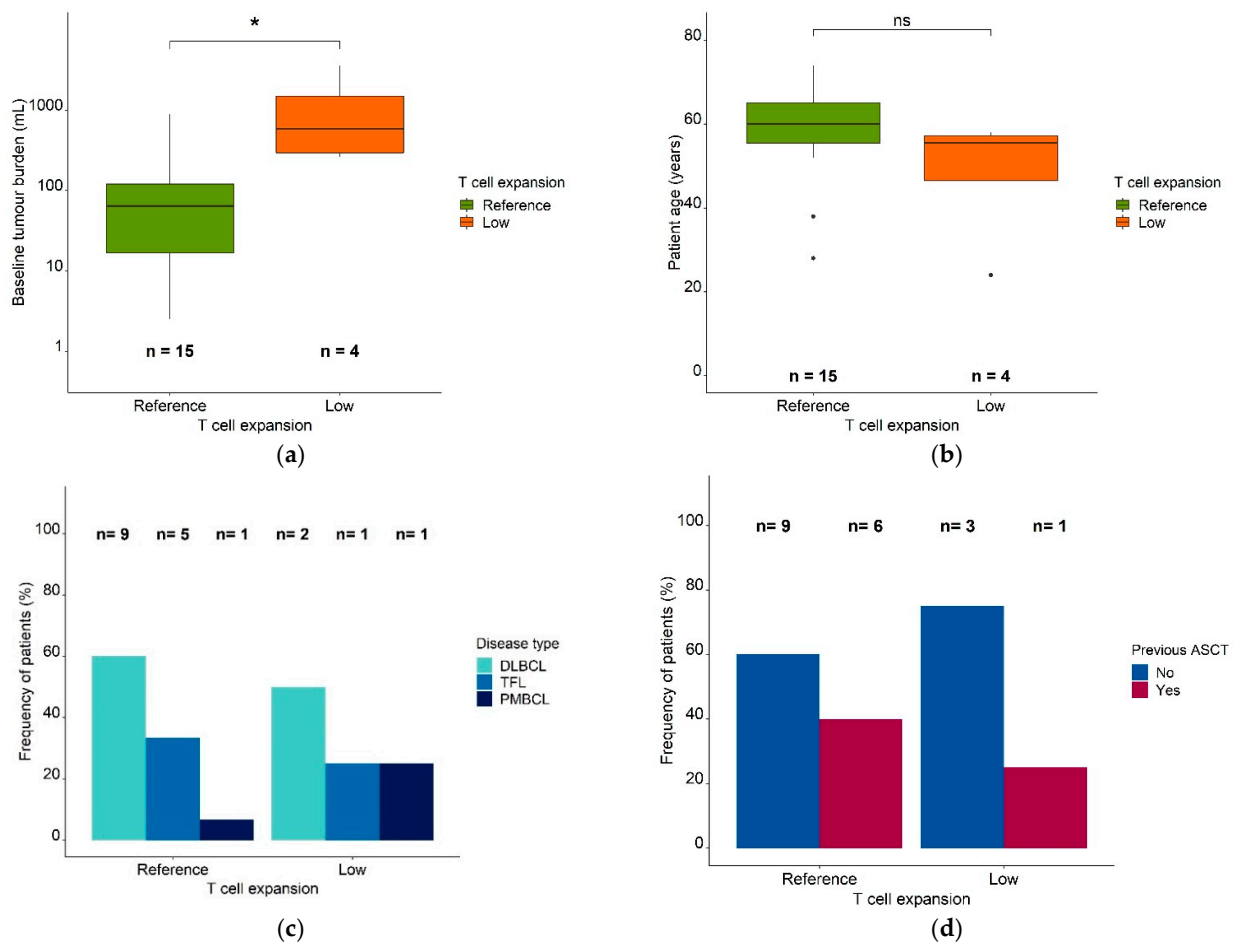


Figure 4. Patient characteristics in the reference expansion population and the low expansion subpopulation. Legend: (a) Baseline metabolic tumor volume (mL) in the reference expansion population and the low expansion subpopulation. (b) Patient age in the reference expansion population and the low expansion subpopulation. Boxes: interquartile range (IQR) including median; whiskers: range from hinge to lowest/highest value within 1.5 IQR; points: data outside whisker. (c) Frequency of patients in the reference expansion population and the low expansion subpopulation, stratified for disease type. (d) Frequency of patients in the reference expansion population and the low expansion subpopulation, stratified for a previous ASCT. Abbreviations—ASCT: autologous stem cell transplantation, DLBCL: diffuse large B cell lymphoma, PMBCL: primary mediastinal B cell lymphoma, TFL: transformed follicular lymphoma, *: $p \leq 0.05$, ns: $p > 0.05$.

There was a high agreement between observations and model predictions for the CAR-T cell kinetic parameters (Figure 5, Supplementary Table S2). C_{\max} and AUC_{0-28d} were similar in reference and low expansion (sub) populations, while T_{\max} were earlier in the reference compared to the low expansion (sub) population. When observed C_{\max} values were normalized to baseline metabolic tumor volumes, these ratios were significantly higher in the reference compared to the low expansion subpopulation ($p = 0.024$).

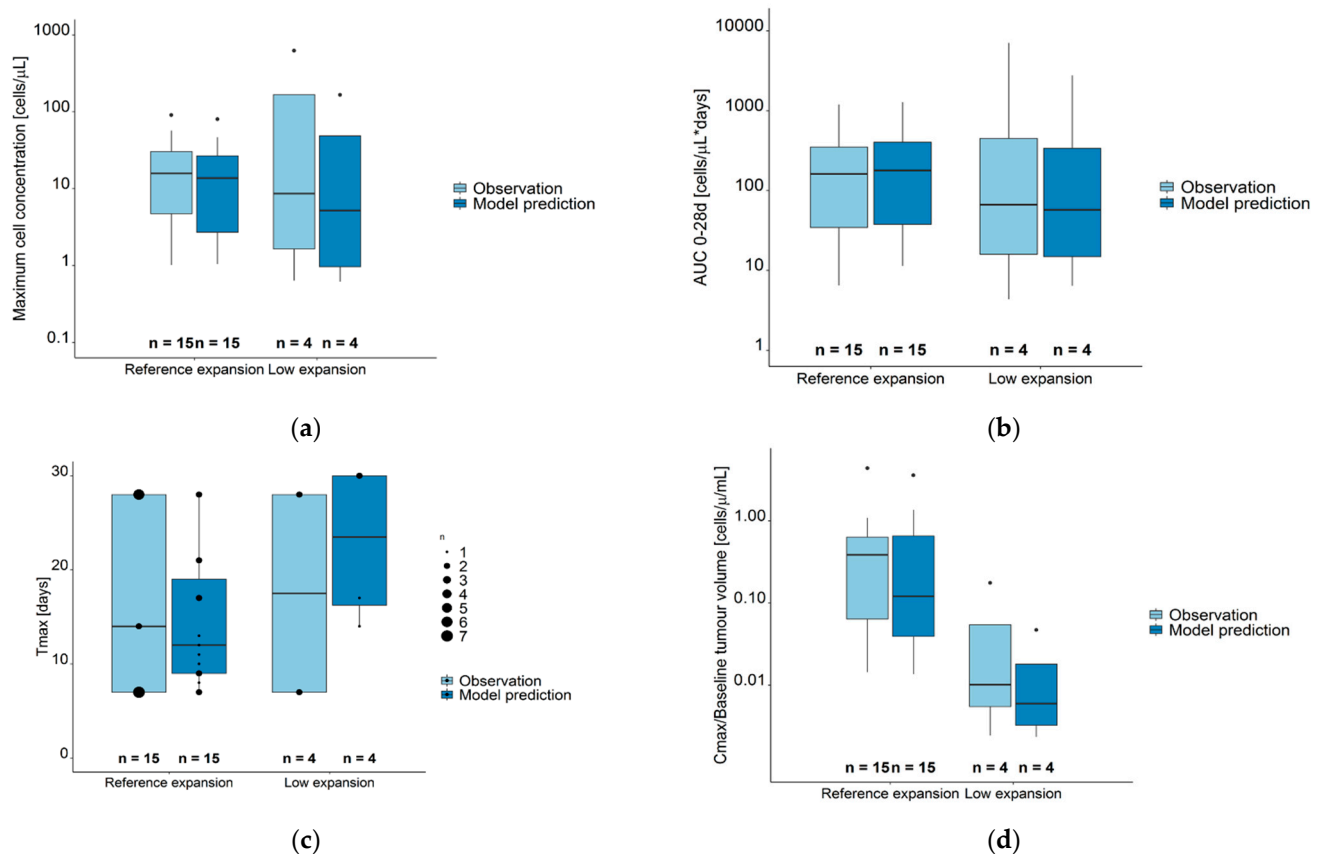


Figure 5. Observed (light blue boxes) and model predicted (dark blue boxes) CAR-T cell kinetic parameters for the sum of all CAR-T cell populations. (a) Maximum cell concentration (C_{\max}). (b) Area under the concentration–time curve from day 0–28 (AUC_{0-28d}). (c) Time at maximum concentration (days); data points of differences sizes mark the number of observations/predictions at different time points. (d) C_{\max} /Baseline metabolic tumor volume ($\text{cells } \mu\text{L}^{-1} \text{ mL}^{-1}$). Legend—Boxes: interquartile range (IQR) including median; whiskers: range from hinge to lowest/highest value within 1.5 IQR; points: data outside whisker. Abbreviations— T_{\max} : time at maximum CAR-T cell concentration; AUC_{0-28d} : area under the concentration–time curve from days 0–28, C_{\max} : maximum CAR-T cell concentration.

3.3. Clinical Endpoints in Different Model-Defined Patient Subpopulations

Compared to the reference population, the low expansion subpopulation had shorter PFS (median: 2.5 months vs. 11 months, $p = 0.31$, Figure 6a) and overall survival (OS) (median: four months vs. not reached, $p = 0.13$, Figure 6b).

Patients having undergone a previous ASCT ($n = 7$) had a significantly longer PFS compared to patients who had not ($n = 12$) (median PFS: Not reached vs. three months, $p = 0.0066$, Figure 7a) and this difference remained in OS (median OS: Not reached vs. six months, $p = 0.0042$, Figure 7b).

We also observed differences in PFS and OS in patients with different combinations of ASCT pre-treatment and T cell expansion capacity (Figure 8a,b): both median PFS and OS in patients in the low expansion subpopulation with no previous ASCT ($n = 3$) were two months.

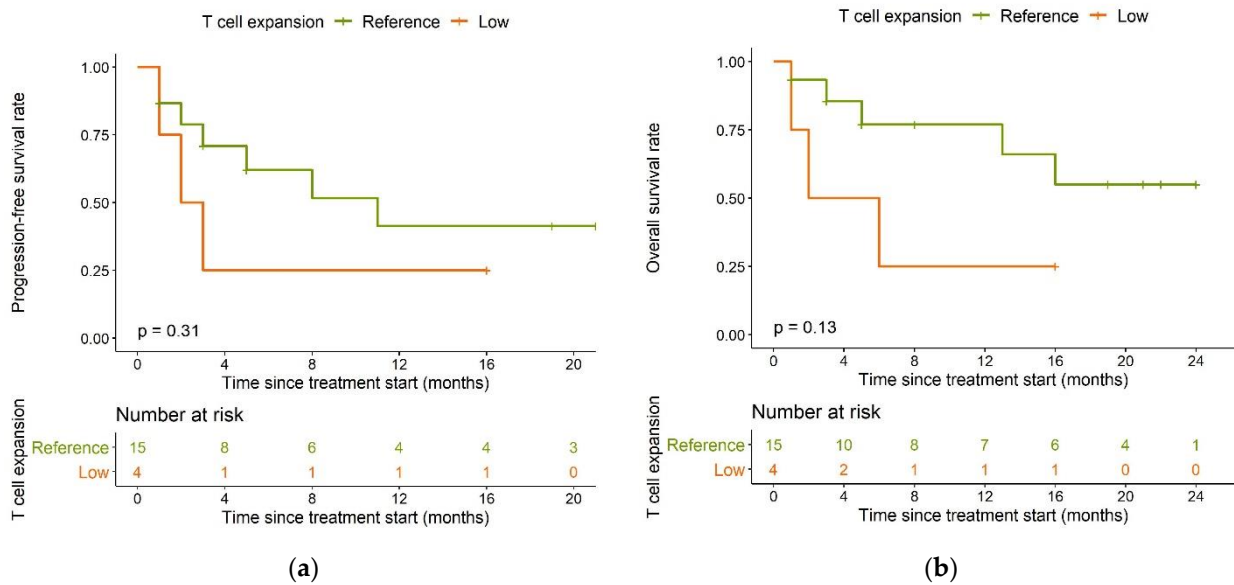


Figure 6. Kaplan–Meier plots for (a) progression-free survival and (b) overall survival in the reference T cell expansion population (green) and the low expansion subpopulation (orange); log-rank tests.

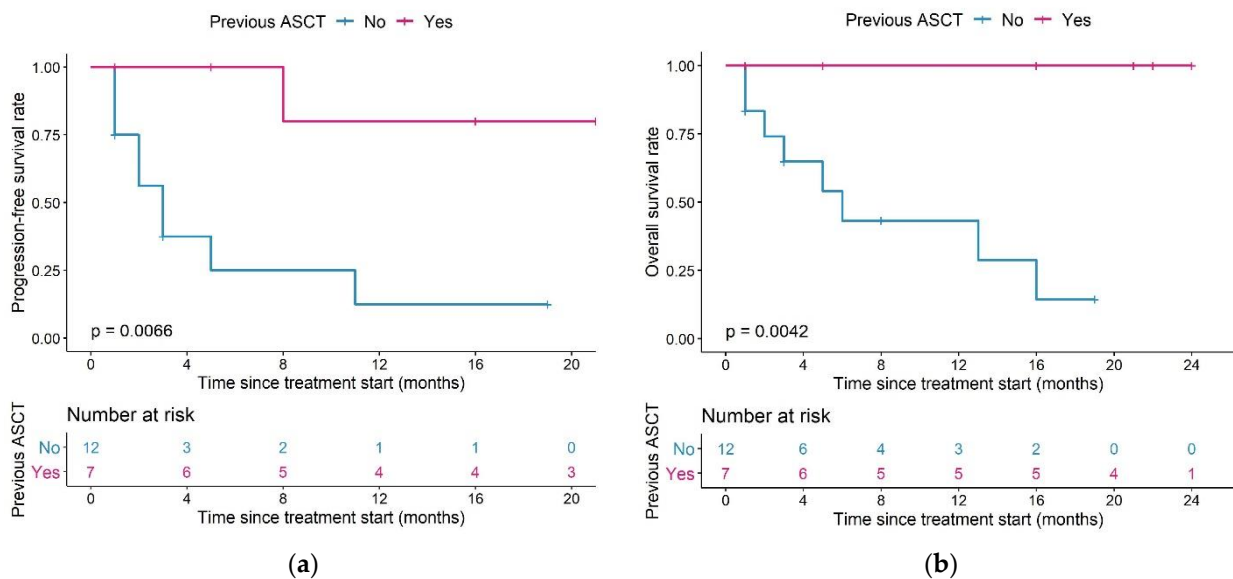


Figure 7. Kaplan–Meier plots for (a) progression-free survival and (b) overall survival in patients having undergone (magenta) or having or not undergone (blue) a previous ASCT; log-rank tests. Abbreviations—ASCT: autologous stem cell transplantation.

For patients in the reference expansion population with no previous ASCT ($n = 9$), median PFS was five months, and median OS was 13 months. In patients with a previous ASCT, both median PFS and OS were not reached in both the reference population ($n = 6$) and the low expansion subpopulation ($n = 1$).

All patients who had undergone previous ASCT ($n = 7$) were still alive after a maximum of 24 months of follow-up. Among patients with no previous ASCT, OS was different between patients in the reference or low expansion (sub)population: 44.4% of patients were still alive in the reference population ($n = 9$), compared to 0% of patients in the low expansion subpopulation ($n = 3$).

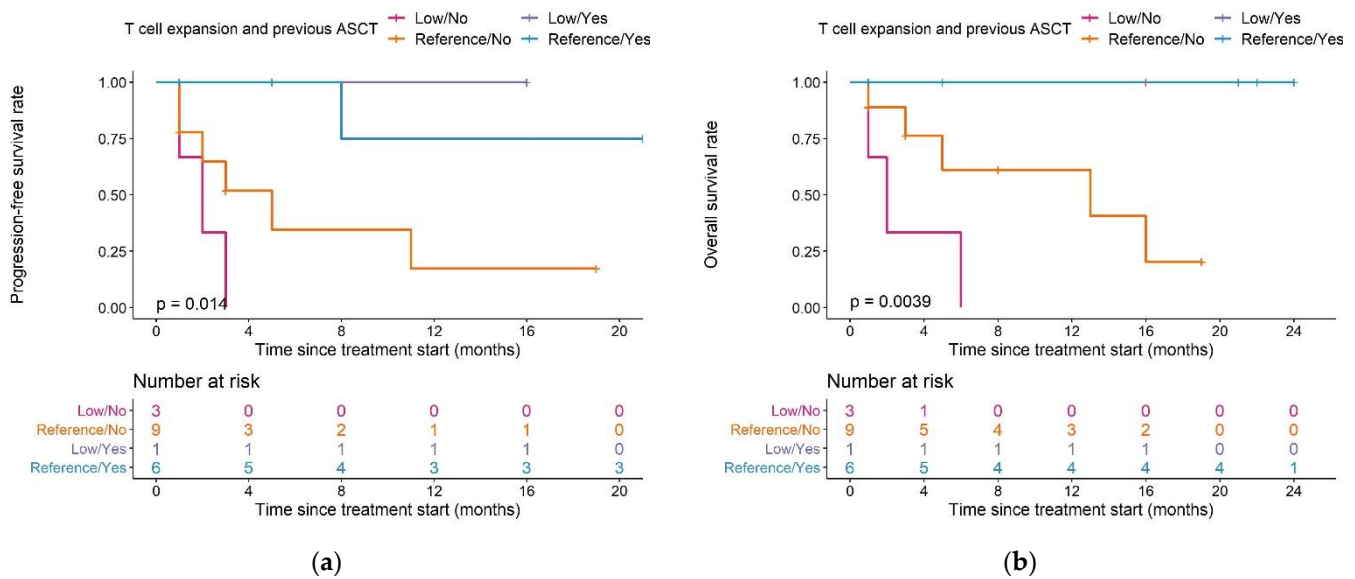


Figure 8. Kaplan–Meier plots for (a) progression-free survival and (b) overall survival in patients with different combinations of T cell expansion and previous ASCT group; log-rank tests. Pairwise comparisons were performed to assess between which curves there was a significant difference (a): significant difference between Reference/Yes and Low/No, $p = 0.019$, (b): significant difference between Reference/Yes and Low/No, $p = 0.026$). Legend—Magenta curve: Patients in the low expansion subpopulation who did not undergo a previous ASCT; orange curve: patients in the normal expansion subpopulation who did not undergo a previous ASCT; purple curve: patients in the low expansion subpopulation who underwent a previous ASCT, blue curve: patients in the reference expansion population who underwent a previous ASCT. Abbreviations—ASCT: autologous stem cell transplantation.

PFS and OS were significantly different between patients in the reference expansion subpopulation who did ($n = 6$) or did not ($n = 9$) undergo ASCT (median PFS and OS: not reached vs. five months ($p = 0.039$) and not reached vs. 13 months ($p = 0.02$), in patients with or without previous ASCT, respectively).

The model-estimated maximum expansion capacity, $V_{\max 1}$, allowed to identify a patient's expansion (sub-)population, which was associated with survival; thus, we aimed to determine a cut-off value in this parameter, which would support survival prediction. Furthermore, we aimed to translate $V_{\max 1}$ into a predictor variable, which would be easily derivable in a clinical setting and leverage, but not require the use of the model. As a measurable clinical composite score (CCS) describing T cell expansion, inspired by a similar concept in anti-PD1 checkpoint blockade [39] and supported by a previous correlative analysis [50], the ratio of observed C_{\max} ((cells· μL^{-1}))/baseline metabolic tumor volume (mL), denoted in Equation (12), was positively correlated with $V_{\max 1}$ for all CAR-T cell phenotypes (T_N : $r = 0.98$, T_{CM} : $r = 0.95$, T_{EM} : $r = 0.94$, T_{EFF} : $r = 0.86$, T_{all} : $r = 0.94$). As the highest correlation was observed for T_N (Figure 9a), the CCS for T_N (CCS_{T_N}) was taken forward as a possible predictor for survival.

$$\text{Clinical composite score (CCS)} = \frac{\text{Maximum CAR - T cell concentration}}{\text{Baseline metabolic tumour volume}} \quad (12)$$

A receiver operator characteristic curve (ROC) analysis determined a CCS_{T_N} of 0.00136 (cells· μL^{-1})·mL $^{-1}$ as cut-off value with optimal predictive capability for patients in the low expansion subpopulation (sensitivity: 75%, specificity: 100%; AUC: 91.7%) (Figure 9b and Supplementary Figure S6). The survival analysis, stratified for the proposed cut-off value, showed a clear superiority in survival in patients with a $CCS_{T_N} \geq 0.00136$ (cells· μL^{-1})·mL $^{-1}$ compared to patients with a CCS below this value (median PFS: 11 months vs. 2 months ($p = 0.014$) and median OS: not reached vs. two months ($p = 0.003$)).

(Figure 9c,d). Using a Cox-proportional hazard model, the estimated hazard ratios for PFS and OS in patients with a CCS_{TN} above the proposed threshold were 0.17 (95% CI: 0.037–0.79) ($p = 0.024$) and 0.12 (95% CI: 0.025–0.63) ($p = 0.012$), respectively, suggesting that a CCS_{TN} above the proposed threshold was associated with a 83% reduced risk of progression and a 88% reduced risk of death.

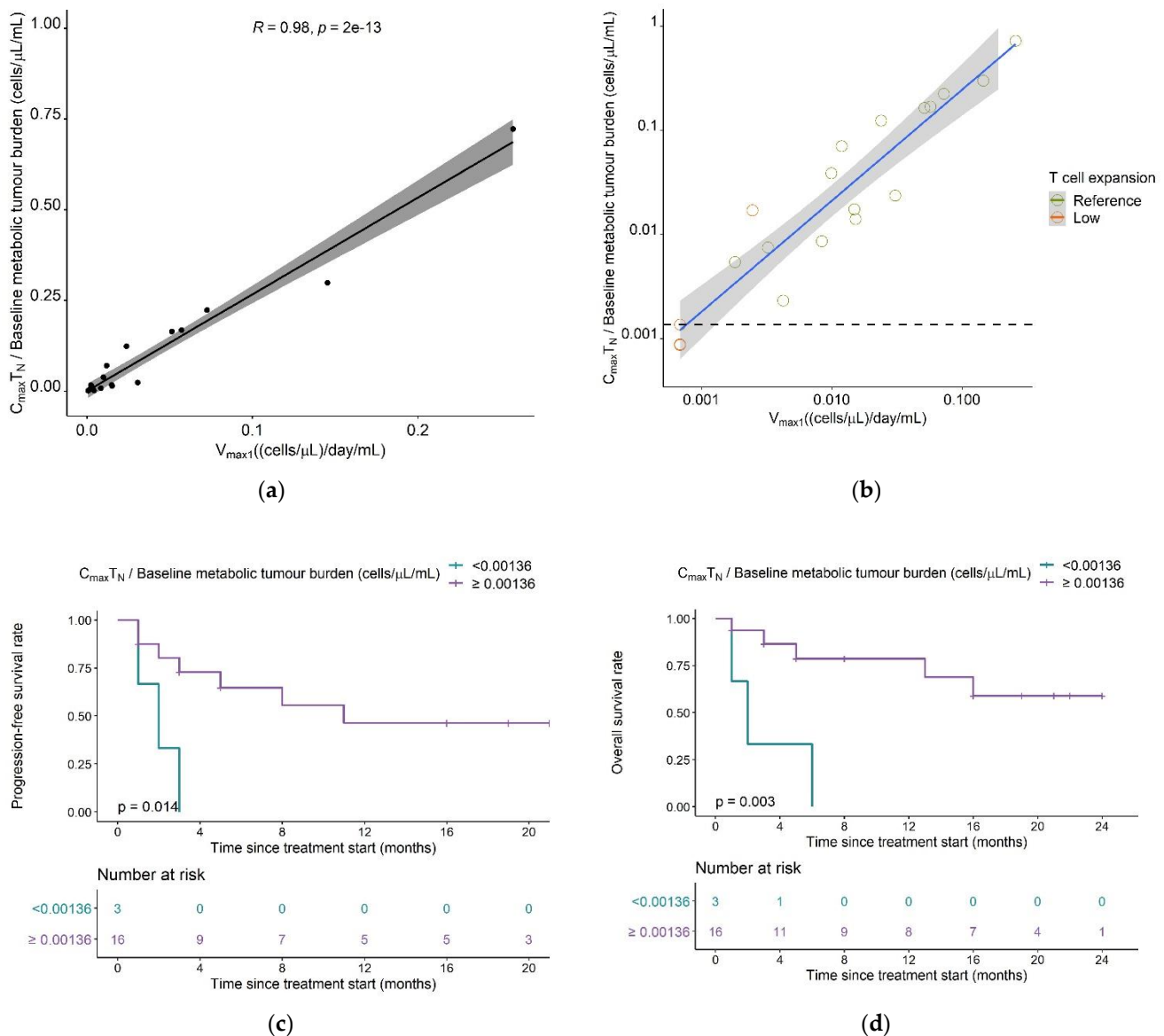


Figure 9. Determination of a clinical composite score (CCS) cut-off value for early response-prediction. **(a)** Correlation between model parameter $V_{max1} ((\text{cells} \cdot \mu\text{L}^{-1}) \cdot \text{day}^{-1} \cdot \text{mL}^{-1})$ and CCS_{TN} Maximum naïve CAR-T cell concentration/Metabolic tumor volume at baseline $((\text{cells} \cdot \mu\text{L}^{-1}) \cdot \text{mL}^{-1})$. **(b)** Correlation plot as **A** but on a log-log scale and different labeling of the T cell expansion subpopulation. The dashed horizontal line marks the CCS_{TN} cut-off value most predictive for allocation to the low expansion subpopulation, as determined using ROC analysis. **(c)** Kaplan–Meier probabilities for progression-free survival in patients below or exceeding the determined CCS_{TN} cut-off value. **(d)** Kaplan–Meier plots for overall survival in patients below or exceeding the determined CCS_{TN} cut-off value. Abbreviations— CCS_{TN} : clinical composite score for naïve CAR-T cells.

Log_{10} -transformed CCS using C_{max} values for all CAR-T cells derived from flow cytometry were reasonably correlated with log -transformed CCS using C_{max} values derived from cfDNA qPCR ($r = 0.48$, $p = 0.037$) and the CCS_{qPCR} values were significantly higher in the reference expansion population compared to the low expansion subpopulation

(median: 83.7 copies μg^{-1} DNA $\cdot\text{mL}^{-1}$ vs. median: 4.16 copies μg^{-1} DNA $\cdot\text{mL}^{-1}$, $p = 0.014$) (Figure 10a,b). Furthermore, CCS_{qPCR} values were significantly higher in patients with complete response/partial response vs. patients with progressive disease/no response in previously digitized data [41] of patients with multiple myeloma [43] ($p = 0.017$) and chronic lymphocytic lymphoma [42] ($p = 0.0051$) (Figure 10c,d), further supporting our clinical composite score framework.

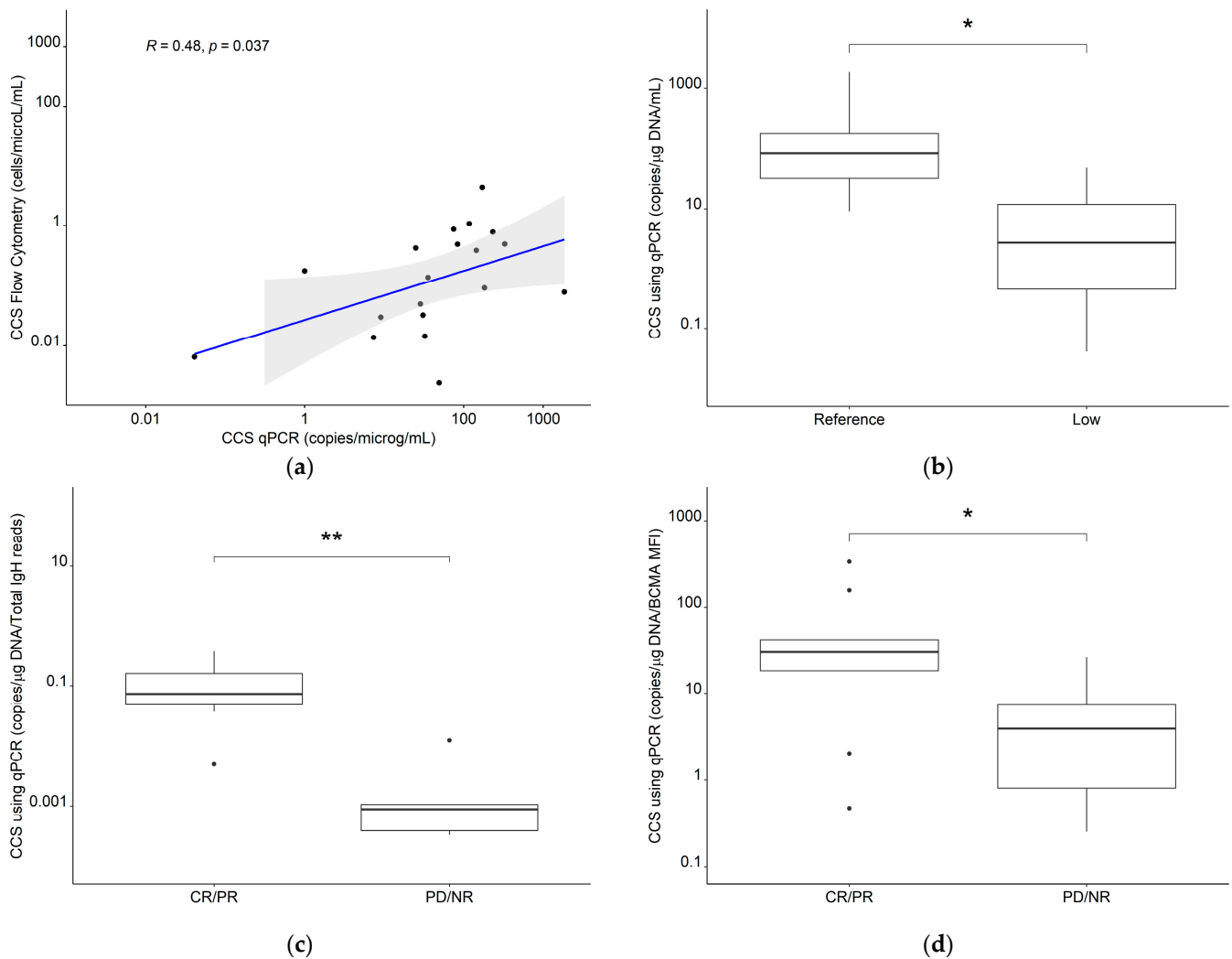


Figure 10. (a) Correlation for the clinical composite score for T_{all} using flow cytometry or qPCR and comparisons of the CCS using qPCR between (b) reference expansion population and low expansion subpopulation in our clinical dataset, (c) CR/PR and PD/NR in CLL patients ($n = 12$) and (d) CR/PR and PD/NR in MM patients ($n = 19$). Abbreviations—CLL: chronic lymphocytic leukemia; CR: complete response; MM: multiple myeloma; NR: no response; PR: partial response; qPCR: quantitative polymerase chain reaction; T_{all} : the sum of all measured CAR-T cell phenotypes. *: $p \leq 0.05$, **: $p \leq 0.01$.

4. Discussion

Leveraging our developed population quantitative systems pharmacology CAR-T cell model, we identified patient characteristics explaining two-thirds of the large interindividual variability observed in the CAR-T cell expansion in our dataset, and these patient characteristics were also partially predictive for survival. Previously reported prognostic factors such as a high maximum CAR-T cell concentration [1,4,7,19,50], a high baseline metabolic tumor volume [50–52], or a high area under the concentration–time curve (AUC) in the first month [4,7,50] were not predictive for overall survival in our clinical cohort (Supplementary Figure S7–S9). Other studies similarly did not find relationships between

outcome and a high maximum CAR-T cell concentration [53], a high baseline tumor burden [5,53], or a high area under the concentration–time curve (AUC) in the first month [53]. Possible reasons for the different findings could be different patient populations, different disease characteristics, different study designs, and/or different CAR-T cell products used. A pooled analysis of the clinical cohorts for which the proposed relationships were found or not found could aid in identifying potential underlying factors of the observed discrepancies. Interestingly, in a recent analysis, there was a stronger association between the probability of durable response and maximum CAR-T cells/tumor burden ($p = 0.0017$) than between the probability of durable response and maximum CAR-T cells ($p = 0.0159$) [50]. This supports our exploratory finding of the maximum CAR-T cell expansion normalized to baseline tumor burden being a more reliable predictor for outcome than maximum CAR-T cell expansion alone. Our exploratory findings and our modeling framework may spark further research regarding the impact of a previous ASCT on CAR-T cell expansion and treatment outcome.

Nonlinear mixed-effects modeling, as applied in the CAR-T cell quantitative systems pharmacology model, allows simultaneously characterizing typical profiles and identifying several layers of variability around the kinetic/dynamic parameters and observations in CAR-T cell therapy. The implementation of covariates aids in explaining parts of the interindividual variability and, thus, can increase the understanding of CAR-T cell therapy. Furthermore, our CAR-T cell modeling framework is flexible and allows the analysis of pooled datasets which offers the possibility to simultaneously leverage the information generated in multiple independent clinical studies. Therefore, especially if applied to a large and diverse clinical dataset, the developed CAR-T cell model is a valuable tool for elucidating influential factors on the kinetics and dynamics of CAR-T cell therapy and treatment outcome.

We based our structural CAR-T cell model on the T cell progressive differentiation model, which describes T cell differentiation in the order of naïve T cells via T memory stem cells (T_{SCM}) over central memory cells, and over effector memory cells to short-lived effector cells. Although other lineage relationship models like the linear differentiation model [54] and the bifurcative differentiation model [55,56] have been proposed, the progressive differentiation model is most supported by experimental data [20,57–61]. Of note, our flow cytometry panel did not include the marker CD95 and thus did not support the detection of T_{SCM} in the presence of T_N . Thus, using an extended staining panel, future studies including cell concentration data of both T_N and T_{SCM} could extend our model, considering previous reports of the positive features of T_{SCM} regarding CAR-T cell expansion and persistence. Additional flow cytometry markers such as TAM-3, LAG3, PD-1, and CD57 could further elucidate the state of the T cell with respect to exhaustion and senescence.

In previous immunotherapy models [29,62,63], T cell expansion upon tumor contact was modeled using a Michaelis–Menten equation with the tumor cell concentration in the denominator. In contrast to this, our data were described best when we used the respective T cell concentration in the denominator. Thus, our model describes that at sufficiently high T cell concentrations, T cell expansion is proportional to the tumor burden, which is in line with another previously described immunotherapy model [28]. Furthermore, this form of the equation correctly described the rapid initial CAR-T cell expansion phase followed by the sharp drop in our observed CAR-T cell concentrations. When using metabolic tumor volume in the denominator, the concentration–time profile in the expansion phase showed a lag-time and a partly mono-exponential decline after the maximum expansion. A possible reason for this could be the low initial imputed CAR-T cell doses of 0.1 cells/ μL , which result in slow expansion if the expansion term postulates that expansion is proportional to the concentration of CAR-T cells at high tumor burdens. Plots for the predicted concentration–time profiles for the base models (i.e., not considering covariates or mixture model) using either metabolic tumor volume or the respective CAR-T cell population in the denominator are shown in Supplementary Figure S10. The expansion term should be revisited once a

larger sample size is available to ensure that expansion can be well-described over a broad range of initial tumor burdens and that no unphysiological expansion rates are postulated. Furthermore, it is possible that using the tumor burden in the denominator as proposed by several other researchers [29,62,63] would describe the trajectory equally well or even better than our suggested term when using individual CAR-T cell concentrations in the pre-distribution phase, and this should be explored upon availability of such data.

Not in our study, but if lymphodepleting chemotherapy was administered in higher doses and for longer than three days, it may exert some decreasing effect on the metabolic tumor volume. A prerequisite for the identification of separate, rapid killing effect parameters to comprehensively characterize this process is data from multiple tumor volume assessments, i.e., prior to and after lymphodepleting chemotherapy.

Based on T cell physiology, we aimed to determine different values for the baseline maximum expansion rate upon tumor contact $V_{\max,base}$ for each phenotype by estimating $V_{\max,base}$ for T_N and fractional changes in $V_{\max,base}$ for the remaining three phenotypes. Point estimates of the fractional changes in $V_{\max,base}$ for each phenotype were plausible (T_{CM} : +24%; T_{EM} : +14%, T_{Eff} : -79%), however, with relative standard errors of 130–583%, the estimates were imprecise. We thus simplified the model by assuming the same $V_{\max,base}$ for T_N , T_{CM} , and T_{EM} and removing the respective expansion term for T_{Eff} . Additional in vivo and in vitro data need to become available for precise estimation of $V_{\max,base}$ parameter values for each CAR-T cell phenotype and for identification of the best CAR-T cell phenotype(s) for the strongest expansion.

We identified two covariates that significantly influenced the baseline maximum expansion rate $V_{\max1,base}$, namely the $CD4^+/CD8^+$ CAR-T cell ratio at day seven and a previous ASCT. By additionally considering if patients showed a reference or low baseline expansion, we could substantially reduce the estimated interindividual variability on $V_{\max1,base,ref}$ by two-thirds from 446% to 150% CV. We identified $V_{\max1,base,ref}$ to moderately decrease with a higher ratio of $CD4^+$ to $CD8^+$ T cells at day seven. This means that we estimated $CD8^+$ T cells to have a higher expansion rate than $CD4^+$ T cells, as reported previously [64]. In contrast, we did not identify covariates that could explain parts of the large interindividual variability on CAR-T cells' maximum tumor killing rate ($V_{\max5}$). While we did find a significant positive relationship between cytokine release syndrome grade ≥ 2 and maximum tumor killing rate by T_{CM} ($V_{\max5,2}$), we think that this relationship is rather due to correlation than causation. A higher immune activation, leading to a higher grade of cytokine release syndrome, might be the reason for the increased killing rate. However, as we aimed for our model to be mechanistic and our data did not include the link (i.e., a biomarker) between cytokine release syndrome and $V_{\max5,2}$, we decided not to include cytokine release syndrome as a covariate on $V_{\max5}$. In general, the units of model parameters $V_{\max1}$, $V_{\max5,2}$, and the CCS could be further transformed by resolving the units, e.g., the different volume units (μL) and (mL). However, to ease interpretability and retain awareness for the different origins of the units (μL) represents the distribution volume of the CAR-T cells and (mL) represents the metabolic tumor volume), the units of the parameters were kept in their original form.

Even though our model described the observed clinical data very well and allowed elucidating sources of interindividual variability, rather high residual unexplained variability of 59–120% CV remained. Data of additional patients and a higher number of samples per patients will allow optimizing parameter estimates and further investigating potential covariates to reduce the residual unexplained variability.

Leveraging our model, we identified a subpopulation with low maximum T cell expansion upon tumor contact. This subpopulation consisted of 20% patients ($n = 4$ of 19) in our dataset, which is comparable to a previous clinical study in which 12% ($n = 5$ of 43 patients) of patients showed low T cell expansion and had a poor prognosis [10]. T cells of these patients showed an increased frequency of $LAG3^+/TNF\alpha_{lo}$ T cells in the manufacturing product and rapid expression of exhaustion markers after infusion. We hypothesize that the same pattern could have been observed in patients of our low

expansion subpopulation. Unfortunately, no exhaustion markers were measured in our dataset, so we were not able to investigate this further, but the generated hypothesis should be tested in future. Furthermore, while we observed strong trends for differences in survival between the model-defined reference expansion and the low expansion (sub)population (PFS: 11 months vs. 2.5 months, OS: not reached vs. four months), the differences were not significant. Among the low expansion subpopulation, there was one individual with a previous ASCT, very high baseline metabolic tumor volume, and ~40-fold higher CAR-T cell C_{max} compared to the mean C_{max} in the other 18 patients. Interestingly, this individual's survival was also much longer than the rest of the low expansion subpopulation (ongoing response at 16 months vs. median PFS and OS of 2 months). Had this patient been excluded from the analysis, the differences in PFS and OS between both (sub)populations would have been highly significant ($p = 0.021$ and 0.0049 , respectively). Thus, future studies with a larger sample size to investigate the cell kinetic-independent impact of ASCT and other factors on survival and the model's potential for response prediction are highly warranted. We subsequently translated our predictive model parameter V_{max1} into clinical composite scores (CCS) of maximum CAR-T cell concentrations/baseline metabolic tumor burden, measurable in the clinic. The excellent correlations between V_{max1} and the CCS for all CAR-T cell subpopulations ($r \geq 0.86$) support our model. The highest concordance between the CCS for T_N ($r = 0.98$) was supported by a previous correlative analysis [50] and allowed us to determine a CCS_{TN} cut-off value for early response prediction.

We are aware of our small sample size, resulting from CAR-T cell therapy being a very new (and expensive) therapy in its infancy of a per se very small patient population; thus, only limited data are available worldwide overall. Furthermore, no exhaustion markers were measured. Yet, the exploratory findings of our QSP model allowed the generation of various hypotheses which should be tested with further data to arise in future. In addition, the model might support the design of those experiments/studies well, i.e., which data to sample at which timepoints, to gain maximal information from the data. Importantly, we achieved precise estimation of model parameters in our cohort and our clinical composite score framework was supported by a recent correlative analysis [50]. Nevertheless, future studies with a larger sample size and measuring exhaustion markers will have to be performed to test our hypotheses, revise, and refine our model parameters and determine a robust CCS cut-off value. The improved outcome observed in our dataset in patients with ASCT also needs to be investigated further in a larger study focusing on whether prior ASCT increases T cell expansion and survival. Possible reasons are beneficial disease characteristics in patients eligible for ASCT, the removal of an immunosuppressive microenvironment [12], and the availability of 'fitter' T cells that have not been damaged by previous cycles of chemotherapy. Concerning the latter point and since not every patient can undergo ASCT, a possible strategy could be to collect T cells before the start of chemotherapy and, depending on treatment response, utilize them for CAR-T cell manufacturing as needed. Furthermore, we hypothesize that a minimal time difference between the last cycle of chemotherapy and T cell collection has to be maintained, allowing T cells to recover and increasing the chance for high T cell fitness in the manufacturing product. Thus, future studies will focus on determining the optimal time differences between the last cycle of chemotherapy and T cell collection and between ASCT and T cell collection. With more data on these aspects to be collected, our QSP model can be expanded to consider the fitness of T cells prior to manufacturing and thus the potential for a robust expansion upon infusion.

Finally, it would be advantageous to predict outcomes before CAR-T cell infusion, or even before CAR-T cell manufacturing. Thus, future studies applying our QSP model on data including (i) patient baseline characteristics, (ii) CAR-T cell fitness in the leukapheresis product, (iii) CAR-T cell fitness in the infusion product, (iv) metabolic tumor volume over time, (v) CAR-T cell concentrations in vivo over time, and (vi) clinical endpoints could identify and quantify further predictors for long-term response and in the best-case scenario allow response prediction before CAR-T cell manufacturing.

5. Conclusions

In conclusion, our innovative quantitative systems pharmacology CAR-T cell model allowed us to describe the concentration–time profiles of different CAR-T cell phenotypes and metabolic tumor volume in a clinical dataset in a coherent framework. Using the model, we identified factors explaining two-thirds of the high interindividual variability in CAR-T cell expansion and survival in our clinical dataset. Once validated in a larger clinical cohort, the developed quantitative systems pharmacology CAR-T cell model can be used to further identify yet unknown factors resulting in the highly variable kinetics and dynamics of CAR-T cell therapy.

Supplementary Materials: The following are available online at <https://www.mdpi.com/article/10.3390/cancers13112782/s1>. Figure S1: Flow cytometry gating strategy for the isolation of CD4⁺ and CD8⁺ CAR-T cells from peripheral blood samples of patients at days 7, 14, and 28 after infusion and identification of the different phenotypes. Figure S2: Digitized data on C_{\max} and Baseline tumor burden in patients with MM and CLL. Figure S3: Measured concentrations and simulated typical and individual model predictions of different species after CAR-T-cell infusion for patients in the low expansion subpopulation before and after implementation of the mixture model. Figure S4: Estimated maximum expansion capacity upon tumor contact parameter $V_{\max 1}$ versus the CD4/CD8 CAR-T cell ratio at day seven. Figure S5: Simulated typical CAR-T cell concentration–time profiles using different initial CAR-T cell concentrations (0.1 cells μL^{-1} as used in our model (light blue) and ten-fold lower (dark blue) or ten-fold higher (purple) and a baseline metabolic tumor volume of 85.7 mL (median baseline metabolic tumor volume in our dataset) (assuming reference covariate values of no previous autologous stem cell transplantation and a CD4/CD8 CAR-T cell ratio of 1). Figure S6: Receiver operating characteristic (ROC) curve for deriving an optimal cut-off value of the clinical composite score (CCS) Maximum CAR-T_N cell concentrations (C_{\max})/Baseline metabolic tumor volume [(cells $\cdot \mu\text{L}^{-1}$) $\cdot \text{mL}^{-1}$] to determine if patients belong to low expansion subpopulation. Figure S7: Kaplan–Meier plots for and progression-free survival and overall survival in patients with high and low metabolic tumor volume in mL at baseline. Figure S8: Kaplan–Meier plots for progression-free survival and overall survival in patients with high (above median) and low (lower or equal to median) maximum CAR-T cell concentrations. Data points: measured concentrations. Figure S9: Kaplan–Meier plots for progression-free survival and overall survival in patients with high (above median) and low (lower or equal to median) $\text{AUC}_{0-28\text{d}}$ CAR-T cell concentrations. Figure S10: Measured CAR-T cell concentrations and predicted concentration–time profiles using base models with different forms of CAR-T cell expansion terms. Table S1: Patient characteristics. Table S2: Observed and predicted CAR-T cell kinetic parameters in the reference population and the low expansion subpopulation.

Author Contributions: Conceptualization, C.Y. and A.M.-S.; methodology, A.M.-S., R.M., W.H. and C.K.; formal analysis, A.M.-S. and N.P.-O.; investigation, A.M.-S., M.R.G., P.S., B.C., N.P.-O. and S.S.N.; writing—original draft preparation, A.M.-S. and N.P.-O.; writing—review and editing, R.M., M.R.G., A.K., W.H., P.S., B.C., S.S.N., C.Y. and C.K.; visualization, A.M.-S.; supervision, C.K., C.Y. and S.S.N. All authors have read and agreed to the published version of the manuscript.

Funding: This work is supported in part by The University of Texas MD Anderson Cancer Support Grant from National Institutes of Health (P30 CA016672) and generous philanthropic contributions to the University of Texas MD Anderson Moon Shots Program. Publication funding provided by Freie Universitaet Berlin. M.R.G. is a Scholar of the Leukemia and Lymphoma Society. P.S. is supported by the Lymphoma Research Foundation Career Development Award.

Institutional Review Board Statement: The study was conducted according to the guidelines of the Declaration of Helsinki and approved by the Institutional Review Board of the MD Anderson Cancer Center (protocol code 2005-0656, approved on 21 September 2005).

Informed Consent Statement: Informed consent was obtained from all subjects involved in the study.

Data Availability Statement: The datasets generated during and/or analyzed during the current study are not publicly available because patients did not provide consent for sharing their data in a public database and this purpose was also not included in the IRB proposal. On reasonable request, the datasets are available from corresponding author SSN. The NONMEM model code for

the population quantitative systems pharmacology CAR-T cell model are available on reasonable request from corresponding author CK.

Acknowledgments: The authors thank the High-Performance Computing Service of ZEDAT at Freie Universitaet Berlin (<https://www.zedat.fu-berlin.de/HPC/Home> (accessed on 12 January 2021), for computing time.

Conflicts of Interest: C.K. and W.H. report grants from an industry consortium (AbbVie Deutschland GmbH & Co. KG, AstraZeneca Ltd., Boehringer Ingelheim Pharma GmbH & Co. KG, Grünenthal GmbH, F. Hoffmann-La Roche Ltd., Merck KGaA and Sanofi) for the PharMetrX PhD program. C.K. reports grants for the Innovative Medicines Initiative-Joint Undertaking, from the Federal Ministry of Education and Research as well as the European Commission, all outside the submitted work. M.R.G reports research funding from Kite, a Gilead Company, Allogene Therapeutics, and Sanofi, honorarium from Tessa Therapeutics, Advisory Board member for Daiichi Sankyo, and stock ownership interest in KDAc Therapeutics. P.S. received research support from AstraZeneca and is a consultant for Roche-Genentech. S.S.N. served as Advisory Board member or consultant for Kite, a Gilead Company, Merck, Bristol-Myers Squibb, Novartis, Celgene, Pfizer, Allogene Therapeutics, Cell Medica/Kuur, Incyte, Precision Biosciences, Legend Biotech, Adicet Bio, Calibr, and Unum Therapeutics; received research support from Kite, a Gilead Company, Bristol-Myers Squibb, Merck, Poseida, Cellectis, Celgene, Karus Therapeutics, Unum Therapeutics, Allogene Therapeutics, Precision Biosciences, and Acerta; received royalties from Takeda Pharmaceuticals; and has intellectual property related to cell therapy. C.Y. serves as Advisory Board member for Immatics US and Berkeley Lights. B.C. serves as Advisory Board member for Advanced Accelerator Applications and Clovis Oncology, both outside of the submitted work. The remaining authors declare that the research was conducted in absence of any commercial or financial relationships that could be construed as a potential conflict of interest.

References

1. Locke, F.L.; Ghobadi, A.; Jacobson, C.A.; Miklos, D.B.; Lekakis, L.J.; Oluwole, O.O.; Lin, Y.; Braunschweig, I.; Hill, B.T.; Timmerman, J.M.; et al. Long-term safety and activity of axicabtagene ciloleucel in refractory large B-cell lymphoma (ZUMA-1): A single-arm, multicentre, phase 1–2 trial. *Lancet Oncol.* **2019**, *20*, 31–42. [[CrossRef](#)]
2. Maude, S.L.; Laetsch, T.W.; Buechner, J.; Rives, S.; Boyer, M.; Bittencourt, H.; Bader, P.; Verneris, M.R.; Stefanski, H.E.; Myers, G.D.; et al. Tisagenlecleucel in Children and Young Adults with B-Cell Lymphoblastic Leukemia. *N. Engl. J. Med.* **2018**, *378*, 439–448. [[CrossRef](#)] [[PubMed](#)]
3. Schuster, S.J.; Bishop, M.R.; Tam, C.S.; Waller, E.K.; Borchmann, P.; McGuirk, J.P.; Jäger, U.; Jaglowski, S.; Andreadis, C.; Westin, J.R.; et al. Tisagenlecleucel in adult relapsed or refractory diffuse large B-cell lymphoma. *N. Engl. J. Med.* **2019**, *380*, 45–56. [[CrossRef](#)] [[PubMed](#)]
4. Neelapu, S.S.; Locke, F.L.; Bartlett, N.L.; Lekakis, L.J.; Miklos, D.B.; Jacobson, C.A.; Braunschweig, I.; Oluwole, O.O.; Siddiqi, T.; Lin, Y.; et al. Axicabtagene Ciloleucel CAR T-Cell Therapy in Refractory Large B-Cell Lymphoma. *N. Engl. J. Med.* **2017**, *377*, 2531–2544. [[CrossRef](#)] [[PubMed](#)]
5. Nastoupil, L.J.; Jain, M.D.; Feng, L.; Spiegel, J.Y.; Ghobadi, A.; Lin, Y.; Dahiya, S.; Lunning, M.; Lekakis, L.; Reagan, P.; et al. Standard-of-care axicabtagene ciloleucel for relapsed or refractory large B-cell lymphoma: Results from the US lymphoma CAR T consortium. *J. Clin. Oncol.* **2020**, *38*, 3119–3128. [[CrossRef](#)]
6. Schuster, S.J.; Bishop, M.R.; Tam, C.S.; Borchmann, P.; Jaeger, U.; Waller, E.K.; Holte, H.; McGuirk, J.; Jaglowski, S.; Tobinai, K.; et al. Long-Term Follow-up of Tisagenlecleucel in Adult Patients with Relapsed or Refractory Diffuse Large B-Cell Lymphoma: Updated Analysis of Juliet Study. *Biol. Blood Marrow Transplant.* **2019**, *25*, S20–S21. [[CrossRef](#)]
7. Mueller, K.T.; Maude, S.L.; Porter, D.L.; Frey, N.; Wood, P.; Han, X.; Waldron, E.; Chakraborty, A.; Awasthi, R.; Levine, B.L.; et al. Cellular kinetics of CTL019 in relapsed / refractory B-cell acute lymphoblastic leukemia and chronic lymphocytic leukemia. *Blood* **2017**, *130*, 2317–2326. [[CrossRef](#)]
8. Guedan, S.; Calderon, H.; Posey, A.D.; Maus, M.V. Engineering and Design of Chimeric Antigen Receptors. *Mol. Ther. Methods Clin. Dev.* **2019**, *12*, 145–156. [[CrossRef](#)]
9. Kaartinen, T.; Luostarinen, A.; Maliniemi, P.; Keto, J.; Arvas, M.; Belt, H.; Koponen, J.; Mäkinen, P.I.; Loskog, A.; Mustjoki, S.; et al. Low interleukin-2 concentration favors generation of early memory T cells over effector phenotypes during chimeric antigen receptor T-cell expansion. *Cytotherapy* **2017**, *19*, 689–702. [[CrossRef](#)]
10. Finney, O.C.; Brakke, H.; Rawlings-Rhea, S.; Hicks, R.; Doolittle, D.; Lopez, M.; Futrell, B.; Orentas, R.J.; Li, D.; Gardner, R.; et al. CD19 CAR T cell product and disease attributes predict leukemia remission durability. *J. Clin. Investig.* **2019**, *129*, 2123–2132. [[CrossRef](#)]
11. Berger, C.; Jensen, M.C.; Lansdorp, P.M.; Gough, M.; Elliott, C.; Riddell, S.R. Adoptive transfer of effector CD8+ T cells derived from central memory cells establishes persistent T cell memory in primates. *J. Clin. Investig.* **2008**, *118*, 294–305. [[CrossRef](#)]

12. Wang, X.; Popplewell, L.L.; Wagner, J.R.; Naranjo, A.; Blanchard, M.S.; Mott, M.R.; Norris, A.P.; Wong, C.W.; Urak, R.Z.; Chang, W.; et al. Phase 1 studies of central memory—derived CD19 CAR T—cell therapy following autologous HSCT in patients with B-cell NHL. *Blood* **2016**, *127*, 2980–2991. [[CrossRef](#)]
13. Turtle, C.J.; Riddell, S.R.; Maloney, D.G.; Turtle, C.J.; Hanafi, L.; Berger, C.; Gooley, T.A.; Cherian, S.; Hudecek, M.; Sommermeyer, D.; et al. CD19 CAR—T cells of defined CD4 +: CD8 + composition in adult B cell ALL patients. *J. Clin. Investig.* **2016**, *126*, 2123–2138. [[CrossRef](#)] [[PubMed](#)]
14. Kodumudi, K.N.; Weber, A.; Sarnaik, A.A.; Pilon-Thomas, S. Blockade of Myeloid-Derived Suppressor Cells after Induction of Lymphopenia Improves Adoptive T Cell Therapy in a Murine Model of Melanoma. *J. Immunol.* **2012**, *189*, 5147–5154. [[CrossRef](#)]
15. Baba, J.; Watanabe, S.; Saida, Y.; Tanaka, T.; Miyabayashi, T.; Koshio, J.; Ichikawa, K.; Nozaki, K.; Koya, T.; Deguchi, K.; et al. Depletion of radio-resistant regulatory T cells enhances antitumor immunity during recovery from lymphopenia. *Blood* **2012**, *120*, 2417–2427. [[CrossRef](#)]
16. Hirayama, A.V.; Gauthier, J.; Hay, K.A.; Voutsinas, J.M.; Wu, Q.; Gooley, T.; Li, D.; Cherian, S.; Chen, X.; Pender, B.S.; et al. The response to lymphodepletion impacts PFS in patients with aggressive non-Hodgkin lymphoma treated with CD19 CAR T cells. *Blood* **2019**, *133*, 1876–1887. [[CrossRef](#)] [[PubMed](#)]
17. Turtle, C.J.; Hanafi, L.A.; Berger, C.; Hudecek, M.; Pender, B.; Robinson, E.; Hawkins, R.; Chaney, C.; Cherian, S.; Chen, X.; et al. Immunotherapy of non-Hodgkin’s lymphoma with a defined ratio of CD8+ and CD4+ CD19-specific chimeric antigen receptor-modified T cells. *Sci. Transl. Med.* **2016**, *8*, 335RA116. [[CrossRef](#)] [[PubMed](#)]
18. Frey, N.V.; Gill, S.; Hexner, E.O.; Schuster, S.; Nasta, S.; Loren, A.; Svoboda, J.; Stadtmauer, E.; Landsburg, D.J.; Mato, A.; et al. Long-term outcomes from a randomized dose optimization study of chimeric antigen receptor modified T cells in relapsed chronic lymphocytic leukemia. *J. Clin. Oncol.* **2020**, *38*, 2862–2871. [[CrossRef](#)]
19. Fehse, B.; Badbaran, A.; Berger, C.; Sonntag, T.; Riecken, K.; Geffken, M.; Kröger, N.; Ayuk, F.A. Digital PCR Assays for Precise Quantification of CD19-CAR-T Cells after Treatment with Axicabtagene Ciloleucel. *Mol. Ther. Methods Clin. Dev.* **2020**, *16*, 172–178. [[CrossRef](#)]
20. Gattinoni, L.; Lugli, E.; Ji, Y.; Pos, Z.; Paulos, C.M.; Quigley, M.F.; Almeida, J.R.; Gostick, E.; Yu, Z.; Carpenito, C.; et al. A human memory T cell subset with stem cell-like properties. *Nat. Med.* **2011**, *17*, 1290–1297. [[CrossRef](#)]
21. Stein, A.M.; Grupp, S.A.; Levine, J.E.; Laetsch, T.W.; Pulsipher, M.A.; Boyer, M.W.; August, K.J.; Levine, B.L.; Tomassian, L.; Shah, S.; et al. Tisagenlecleucel Model-Based Cellular Kinetic Analysis of Chimeric Antigen Receptor–T Cells. *CPT Pharmacomet. Syst. Pharmacol.* **2019**, *8*, 285–295. [[CrossRef](#)]
22. Singh, A.P.; Zheng, X.; Lin-Schmidt, X.; Chen, W.; Carpenter, T.J.; Zong, A.; Wang, W.; Heald, D.L. Development of a quantitative relationship between CAR-affinity, antigen abundance, tumor cell depletion and CAR-T cell expansion using a multiscale systems PK-PD model. *MAbs* **2020**, *12*, 1688616. [[CrossRef](#)]
23. Kimmel, G.J.; Locke, F.L.; Altrock, P.M. Evolutionary Dynamics of CAR T Cell Therapy. *bioRxiv* **2019**, 717074. [[CrossRef](#)]
24. Chaudhury, A.; Zhu, X.; Chu, L.; Goliaei, A.; June, C.H.; Kearns, J.D.; Stein, A.M. Chimeric Antigen Receptor T Cell Therapies: A Review of Cellular Kinetic-Pharmacodynamic Modeling Approaches. *J. Clin. Pharmacol.* **2020**, *60*, S147–S159. [[CrossRef](#)]
25. Tylutki, Z.; Polak, S.; Wiśniowska, B. Top-down, Bottom-up and Middle-out Strategies for Drug Cardiac Safety Assessment via Modeling and Simulations. *Curr. Pharmacol. Rep.* **2016**, *2*, 171–177. [[CrossRef](#)]
26. Helmlinger, G.; Sokolov, V.; Peskov, K.; Hallow, K.M.; Kosinsky, Y.; Voronova, V.; Chu, L.; Yakovleva, T.; Azarov, I.; Kaschek, D.; et al. Quantitative Systems Pharmacology: An Exemplar Model-Building Workflow with Applications in Cardiovascular, Metabolic, and Oncology Drug Development. *CPT Pharmacomet. Syst. Pharmacol.* **2019**, *8*, 380–395. [[CrossRef](#)]
27. Cheson, B.D.; Fisher, R.I.; Barrington, S.F.; Cavalli, F.; Schwartz, L.H.; Zucca, E.; Lister, T.A. Recommendations for initial evaluation, staging, and response assessment of hodgkin and non-hodgkin lymphoma: The lugano classification. *J. Clin. Oncol.* **2014**, *32*, 3059–3067. [[CrossRef](#)] [[PubMed](#)]
28. Kirschner, D.; Panetta, J.C. Modeling immunotherapy of the tumor—Immune interaction. *J. Math. Biol.* **1998**, *37*, 235–252. [[CrossRef](#)] [[PubMed](#)]
29. Kutznetsov, V.A.; Makalkin, I.A.; Taylor, M.A.; Perelson, A.S. Nonlinear dynamics of immunogenic tumors: Parameter estimation and global bifurcation analysis. *Bull. Math. Biol.* **1994**, *56*, 295–321. [[CrossRef](#)]
30. Owen, J.S.; Fiedler-Kelly, J. *Introduction to Population Pharmacokinetic/Pharmacodynamic Analysis with Nonlinear Mixed Effects Models*, 1st ed.; John Wiley & Sons, Ltd.: Hoboken, NJ, USA, 2014.
31. Mould, D.R.; Upton, R.N. Basic concepts in population modeling, simulation, and model-based drug development. *CPT Pharmacomet. Syst. Pharmacol.* **2012**, *1*, 1–14. [[CrossRef](#)] [[PubMed](#)]
32. Mould, D.R.; Upton, R.N. Basic concepts in population modeling, simulation, and model-based drug development—Part 2: Introduction to pharmacokinetic modeling methods. *CPT Pharmacomet. Syst. Pharmacol.* **2013**, *2*. [[CrossRef](#)]
33. Bauer, R.J. NONMEM Tutorial Part I: Description of Commands and Options, With Simple Examples of Population Analysis. *CPT Pharmacomet. Syst. Pharmacol.* **2019**, 1–13. [[CrossRef](#)] [[PubMed](#)]
34. Bauer, R.J. NONMEM Tutorial Part II: Estimation Methods and Advanced Examples. *CPT Pharmacomet. Syst. Pharmacol.* **2019**, *8*, 538–556. [[CrossRef](#)] [[PubMed](#)]
35. Carlsson, K.C.; Savi, R.M.; Hooker, A.C.; Karlsson, M.O. Modeling subpopulations with the \$MIXTURE subroutine in NONMEM: Finding the individual probability of belonging to a subpopulation for the use in model analysis and improved decision making. *AAPS J.* **2009**, *11*, 148–154. [[CrossRef](#)] [[PubMed](#)]

36. Dosne, A.G.; Bergstrand, M.; Karlsson, M.O. An automated sampling importance resampling procedure for estimating parameter uncertainty. *J. Pharmacokinet. Pharmacodyn.* **2017**, *44*, 509–520. [[CrossRef](#)]
37. Lindbom, L.; Pihlgren, P.; Jonsson, E.; Pihlgren, P.; Jonsson, E.N. PsN-Toolkit—A collection of computer intensive statistical methods for non-linear mixed effect modeling using NONMEM. *Comput. Methods Programs Biomed.* **2005**, *79*, 241–257. [[CrossRef](#)] [[PubMed](#)]
38. Keizer, R.J.; Karlsson, M.O.; Hooker, A. Modeling and simulation workbench for NONMEM: Tutorial on Pirana, PsN, and Xpose. *CPT Pharmacomet. Syst. Pharmacol.* **2013**, *2*, 1–9. [[CrossRef](#)] [[PubMed](#)]
39. Huang, A.C.; Postow, M.A.; Orlowski, R.J.; Mick, R.; Bengsch, B.; Manne, S.; Xu, W.; Harmon, S.; Giles, J.R.; Wenz, B.; et al. T-cell invigoration to tumour burden ratio associated with anti-PD-1 response. *Nature* **2017**, *545*, 60–65. [[CrossRef](#)]
40. Turck, N.; Vutsits, L.; Sanchez-Pena, P.; Robin, X.; Hainard, A.; Gex-Fabry, M.; Fouda, C.; Bassem, H.; Mueller, M.; Lisacek, F.; et al. pROC: An open-source package for R and S+ to analyze and compare ROC curves. *BMC Bioinform.* **2011**, *8*, 12–77. [[CrossRef](#)]
41. Liu, C.; Ayyar, V.S.; Zheng, X.; Chen, W.; Zheng, S.; Mody, H.; Wang, W.; Heald, D.; Singh, A.P.; Cao, Y. Model-Based Cellular Kinetic Analysis of Chimeric Antigen Receptor-T Cells in Humans. *Clin. Pharmacol. Ther.* **2020**, *109*, 716–727. [[CrossRef](#)]
42. Porter, D.L.; Hwang, W.-T.; Frey, N.V.; Lacey, S.F.; Shaw, P.A.; Loren, A.W.; Bagg, A.; Marcucci, K.T.; Shen, A.; Gonzalez, V.; et al. Chimeric antigen receptor T cells persist and induce sustained remissions in relapsed refractory chronic lymphocytic leukemia. *Sci. Transl. Med.* **2015**, *7*, 303ra139. [[CrossRef](#)] [[PubMed](#)]
43. Cohen, A.D.; Garfall, A.L.; Stadtmauer, E.A.; Melenhorst, J.J.; Lacey, S.F.; Lancaster, E.; Vogl, D.T.; Weiss, B.M.; Dengel, K.; Nelson, A.; et al. B cell maturation antigen-specific CAR T cells are clinically active in multiple myeloma. *J. Clin. Investig.* **2019**, *129*, 2210–2221. [[CrossRef](#)] [[PubMed](#)]
44. Chang, J.T.; Wherry, E.J.; Goldrath, A.W. Molecular regulation of effector and memory T cell differentiation. *Nat. Immunol.* **2014**, *15*, 1104–1115. [[CrossRef](#)] [[PubMed](#)]
45. Gett, A.V.; Sallusto, F.; Lanzavecchia, A.; Geginat, J. T cell fitness determined by signal strength. *Nat. Immunol.* **2003**, *4*, 355–360. [[CrossRef](#)]
46. Lanzavecchia, A.; Sallusto, F. Progressive differentiation and selection of the fittest in the immune response. *Nat. Rev. Immunol.* **2002**, *2*, 982–987. [[CrossRef](#)]
47. Macallan, D.C.; Busch, R.; Asquith, B.; Macallan, D.C.; Busch, R.; Asquith, B. Current Estimates of T Cell Kinetics in Humans. *Curr. Opin. Syst. Biol.* **2019**, *18*, 77–86. [[CrossRef](#)]
48. Gattinoni, L.; Klebanoff, C.A.; Restifo, N.P. Paths to stemness: Building the ultimate antitumour T cell. *Nat. Rev. Cancer* **2012**, *12*, 671–684. [[CrossRef](#)]
49. Schmueck-Henneresse, M.; Omer, B.; Shum, T.; Tashiro, H.; Mamonkin, M.; Lapteva, N.; Sharma, S.; Rollins, L.; Dotti, G.; Reinke, P.; et al. Comprehensive Approach for Identifying the T Cell Subset Origin of CD3 and CD28 Antibody-Activated Chimeric Antigen Receptor-Modified T Cells. *J. Immunol.* **2017**, *199*, 348–362. [[CrossRef](#)]
50. Locke, F.L.; Rossi, J.M.; Neelapu, S.S.; Jacobson, C.A.; Miklos, D.B.; Ghobadi, A.; Oluwole, O.O.; Reagan, P.M.; Lekakis, L.J.; Lin, Y.; et al. Tumor burden, inflammation, and product attributes determine outcomes of axicabtagene ciloleucel in large B-cell lymphoma. *Blood Adv.* **2020**, *4*, 4898–4911. [[CrossRef](#)]
51. Dean, E.A.; Mhaskar, R.S.; Lu, H.; Mousa, M.S.; Krivenko, G.S.; Lazaryan, A.; Bachmeier, C.A.; Chavez, J.C.; Nishihori, T.; Davila, M.L.; et al. High metabolic tumor volume is associated with decreased efficacy of axicabtagene ciloleucel in large B-cell lymphoma. *Blood Adv.* **2020**, *4*, 3268–3276. [[CrossRef](#)]
52. Vercellino, L.; Di Blasi, R.; Kanoun, S.; Tessoulin, B.; Rossi, C.; D’Aveni-Piney, M.; Obéric, L.; Bodet-Milin, C.; Bories, P.; Olivier, P.; et al. Predictive factors of early progression after CAR T-cell therapy in relapsed/refractory diffuse large B-cell lymphoma. *Blood Adv.* **2020**, *4*, 5607–5615. [[CrossRef](#)]
53. Awasthi, R.; Pacaud, L.; Waldron, E.; Tam, C.S.; Jäger, U.; Borchmann, P.; Jaglowski, S.; Foley, S.R.; Van Besien, K.; Wagner-Johnston, N.D.; et al. Tisagenlecleucel cellular kinetics, dose, and immunogenicity in relation to clinical factors in relapsed/refractory DLBCL. *Blood Adv.* **2020**, *4*, 560–572. [[CrossRef](#)]
54. Wherry, E.J.; Teichgräber, V.; Becker, T.C.; Masopust, D.; Kaech, S.M.; Antia, R.; von Andrian, U.H.; Ahmed, R. Lineage relationship and protective immunity of memory CD8T cell subsets. *Nat. Immunol.* **2003**, *4*, 225–234. [[CrossRef](#)]
55. Chang, J.T.; Ciocca, M.L.; Kinjyo, I.; Palanivel, V.R.; McClurkin, C.E.; DeJong, C.S.; Mooney, E.C.; Kim, J.S.; Steinel, N.C.; Oliaro, J.; et al. Asymmetric Proteasome Segregation as a Mechanism for Unequal Partitioning of the Transcription Factor T-bet during T Lymphocyte Division. *Immunity* **2011**, *34*, 492–504. [[CrossRef](#)]
56. Chang, J.T.; Palanivel, V.R.; Kinjyo, I.; Schambach, F.; Intlekofer, A.M.; Banerjee, A.; Longworth, S.A.; Vinup, K.E.; Mrass, P.; Oliaro, J.; et al. Asymmetric T lymphocyte division in the initiation of adaptive immune responses. *Science* **2007**, *315*, 1687–1691. [[CrossRef](#)] [[PubMed](#)]
57. Appay, V.; Dunbar, P.R.; Callan, M.; Klenerman, P.; Gillespie, G.M.A.; Papagno, L.; Ogg, G.S.; King, A.; Lechner, F.; Spina, C.A.; et al. Memory CD8+T cells vary in differentiation phenotype in different persistent virus infections. *Nat. Med.* **2002**, *8*, 379–385. [[CrossRef](#)] [[PubMed](#)]
58. Papagno, L.; Spina, C.A.; Marchant, A.; Salio, M.; Rufer, N.; Little, S.; Dong, T.; Chesney, G.; Waters, A.; Easterbrook, P.; et al. Immune activation and CD8+ T-cell differentiation towards senescence in HIV-1 infection. *PLoS Biol.* **2004**, *2*. [[CrossRef](#)] [[PubMed](#)]

59. Sallusto, F.; Lenig, D.; Förster, R.; Lipp, M.; Lanzavecchia, A. Two subsets of memory T lymphocytes with distinct homing potentials and effector functions. *Nature* **1999**, *14*, 708–712. [[CrossRef](#)] [[PubMed](#)]
60. Willinger, T.; Freeman, T.; Hasegawa, H.; McMichael, A.J.; Callan, M.F.C. Molecular Signatures Distinguish Human Central Memory from Effector Memory CD8 T Cell Subsets. *J. Immunol.* **2005**, *175*, 5895–5903. [[CrossRef](#)]
61. Holmes, S.; He, M.; Xu, T.; Lee, P.P. Memory T cells have gene expression patterns intermediate between naïve and effector. *Proc. Natl. Acad. Sci. USA* **2005**, *102*, 5519–5523. [[CrossRef](#)] [[PubMed](#)]
62. De Pillis, L.G.; Radunskaya, A.E.; Wiseman, C.L. A validated mathematical model of cell-mediated immune response to tumor growth. *Cancer Res.* **2005**, *65*, 7950–7958. [[CrossRef](#)] [[PubMed](#)]
63. De Boer, R.J.; Perelson, A.S. Quantifying T lymphocyte turnover. *J. Theor. Biol.* **2013**, *327*, 45–87. [[CrossRef](#)] [[PubMed](#)]
64. Macallan, D.C.; Asquith, B.; Irvine, A.J.; Wallace, D.L.; Worth, A.; Ghattas, H.; Zhang, Y.; Griffin, G.E.; Tough, D.F.; Beverley, P.C. Measurement and modeling of human T cell kinetics. *Eur. J. Immunol.* **2003**, *33*, 2316–2326. [[CrossRef](#)] [[PubMed](#)]